University of Iceland
Faculty of Natural Sciences
Department of Physics

RH-13-2001

THERMAL STRUCTURE OF MAGNETIZED NEUTRON STARS

Óskar Halldórsson Holm

A thesis submitted in partial fulfillment of the
requirements for the degree of
Master of Science in Physics at the University of Iceland

Committee in charge:
Prof. Einar H. Guðmundsson, chair
Research Prof. Gunnlaugur Björnsson

Reykjavík
August 2001

Contents

Abstract

We present the results of numerical calculations of the thermal structure of magnetized neutron star envelopes and find the relationship between the star's (effective) surface temperature and the temperature of the core. A description of the physical conditions in magnetized neutron star envelopes is given, with particular emphasis on the equation of state and the opacity of matter in strong magnetic fields. We describe our numerical methods and calculations in detail and investigate the effects of the various parameters on the results. Fitting formulae for the surface-core temperature relationship are obtained and compared to the results of previous authors.

Chapter 1

Introduction

Neutron stars are among the most exotic objects in the universe. With all of their mass (typically, $M_{\rm NS} \sim M_{\odot}$) pressed into a sphere ~ 10 km in radius, neutron stars host matter in the densest form known, virtually on the brink of a total gravitational collapse. The average density of a typical neutron star of mass $M_{\rm ns} = M_{\odot}$ and radius $R_{\rm ns} = 15$ km is $\rho_{\rm av} \sim 10^{14}$ g/cm^3, comparable to the density inside atomic nuclei. The gravitational fields at neutron star surfaces are therefore extremely strong and outside the range where Newtonian mechanics can be applied. Even more exotic are the extreme magnetic fields that neutron stars harbour. These fields are typically in the range of $10^{12} - 10^{13}$ G. They are therefore huge compared to the Earth's 0.5 G or even the $\sim 10^4$ G fields found in sunspots. The magnetic fields in neutron stars play a large role in their detectability and have a significant effect on their surface structure.

A neutron star is formed in a cataclysmic supernova explosion at the endpoint of stellar evolution, when its massive ($M_* \gtrsim 10 M_{\odot}$) progenitor star has exhausted its supply of nuclear fuel. Unable to withstand its self-gravitation, the stellar core collapses. During the collapse, the density, temperature and pressure in the core rise rapidly until they reach a critical level when the dense nuclear matter forms an incompressible fluid. At that point, the gravitational collapse is abruptly halted. The outer layers come cascading onto the compact core and bounce back, exploding outwards in a spectacular supernova [23], [13]. The stellar core that is left behind has only a fraction of the original star's mass densely packed in a tiny, very hot sphere. The magnetic field of the former star is probably trapped in the core during the collapse and thus magnified (the mechanism through which this occurs is, however, unknown).

First observed by chance in 1967, neutron stars still hold many fascinating mysteries. Chief among the unsolved questions is the one of the physics and composition of the extremely dense cores. Numerous theories on the composition of matter in the cores have been put forth. Suggestions range from quark matter to Hyperons and to Kaon or Pion condensates. The conditions in neutron star cores are far beyond the reach for terrestrial experiments and the physics at these conditions is therefore not well understood. For example, different core models predict greatly differing neutrino production. Since the mean free path of a neutrino in a neutron star core is of the order of the neutron star radius, the neutrinos escape the star and act simply as a heat sink. Therefore, neutrino production is strongly coupled to the cooling rate of the star [17]. This gives us a method to identify the right core model (or at least to rule out wrong models) by comparing the predicted cooling rate of each model to observations of age and core temperature of neutron stars (see discussion in [20] and references therein).

The age of a neutron star can be deduced approximately from observation of changes in the star's spin period. Since there is a limit to how fast the star can spin at birth without breaking apart and since we can assume that the spin-down rate is close to constant throughout the star's life, an estimate of a neutron star's age is simply the time it took the star's rotational period to slow down from the maximum spin rate to today's observed value.

Because a neutron star's core is hidden from view, shrouded in an opaque, thermally insulating envelope, its temperature cannot be measured directly. Rather, the core temperature must be calculated by integrating thermal transport equations from the surface through the envelope. This is the kind of calculations that are presented in this work and they will be explained in the following chapters. For now, we will only note that to apply these calculations to a given neutron star, its surface temperature, surface gravity and magnetic field must be known.

Thermal radiation from neutron star surfaces has proven very difficult to measure. It is relatively faint and peaks in the X-ray part of the spectrum to which the Earth's atmosphere is opaque. Until recently, all observations of neutron stars were indirect, i.e. only photons originating from the environment of neutron stars, e.g. from their magneto-spheres, accretion disks or a companion stars, had been observed. Radio pulsars, for example, are neutron stars that emit a magnetically focused beam of radio photons that originate from electrons being accelerated from the star's magnetic poles by an induced electric field. Pulsars seem to blink at us because as the star rotates, the beam sweeps regularly past the Earth (much like the light from a lighthouse seems to blink at a ship). Similarly, X-ray pulsars are accreting neutron stars in a close binary system with a giant star. The pulsed X-ray emission originates when matter from the giant star is funnelled onto the magnetic poles of the neutron star by its intense magnetic field.

Although more than a thousand radio pulsars, as well as many X-ray pulsars, are known, it has proven very difficult to observe their surfaces directly. Only a few (~ 10) neutron stars have been observed in the optical, UV or soft X-ray ranges [2]. It was only recently, thanks to orbiting X-ray observatories, that thermal photons from neutron star surfaces have been directly observed [3]. Presently, the Chandra X-Ray Observatory is yielding far more detailed observations of the surfaces of isolated neutron stars. These observations are important since they provide astronomers with an estimate of neutron star surface temperatures (see e.g. Page [16] for a discussion on linking the observed spectra to the surface temperature).

In this work we will address the problem of calculating the relationship between the surface temperature, which in many cases can now be observed directly, and the internal temperature, which is related to the star's cooling rate. We will follow closely the method introduced and used by Gudmundsson et al. [8] for non-magnetic neutron stars. Their method is based on the division of neutron stars into two regimes: a thermally isolating envelope and an isothermal core. We will build upon their work and consider the effects of a magnetic field which introduces anisotropy to the problem.

Recent observations indicate that some X-ray pulsars and soft gamma-ray repeaters are *magnetars*, neutron stars with enormous magnetic fields ($B \sim 10^{14} - 10^{15}$ G) [25]. We will not consider such stars in this work, confining our discussion to the cases where $B = 10^{10}, 10^{11}, 10^{12}$, and 10^{13} G.

Several authors have performed similar calculations as presented here. For example, Hernquist [11] calculates the thermal structure for $B \leq 10^{14}$ G for transport along the field. Heyl & Hernquist [12] perform a nearly analytic investigation of the case of a super-strong magnetic field (10^{14} G$\leq B \leq 10^{16}$ G). Van Riper [15], studies the thermal profiles in the parallel case for $B = 10^{10}$–10^{13}. The most recent calculations are those of Potekhin & Yakovlev [20], who calculate thermal structures of neutron star envelopes for both parallel and orthogonal magnetic fields, using modern data for the equation of state and the opacities.

In this work we complement the previous calculations by using a new equation of state for magnetic neutron star envelopes by Thorolfsson et al. [26]. Among other things, we extend the results to lower magnetic fields both for the parallel and orthogonal cases.

The structure of this work is as follows. In chapter 2 we give a brief, general description of the structure of neutron stars, introduce the plane parallel approximation and derive our method for calculating the core temperature. In chapters 3 and 4 we give a detailed explanation of the equation of state and opacity used in our calculations. In chapter 5 we discuss the details of our numerical calculations. We present and analyze our results in chapter 6 and, finally, in chapter 7, we give a brief summary of this work and the results obtained.

Chapter 2

The Thermal Structure of Neutron Stars

In this chapter we give a brief overview of the properties of matter inside neutron stars, present the equations that govern their thermal structure and discuss their division into envelope and interior.

2.1 The Layers of Neutron Stars

A few days after their birth, when their internal temperature has fallen below $\sim 10^9$ K, neutron stars have settled down to a layered structure (see e.g. [13] and [26]).

At the top of an isolated neutron star lies a thin ($\sim$ 10 cm) and tenuous ($\lesssim 10^{-2}$ g/cm^3) *atmosphere*. This atmosphere is responsible for the lines in the spectrum of the thermal radiation originating from the stellar surface. Depending on whether or not the star has accreted matter, the composition of the atmosphere can range from hydrogen to iron. Since the atmospheres are practically isothermal, their presence will not affect the result of this work.

The *envelope*[1] starts just below the atmosphere at an optical depth of 2/3. This is a thin (typically $\sim$ 100 m), opaque and thermally insulating layer composed of ions and a electrons. The composition of the nuclei is density dependent. When the density exceeds $\sim 10^6$ g/cm^3, the electrons (by then degenerate) become relativistic

[1] The layer we refer to as the envelope is sometimes called the *outer envelope* or the *outer crust*.

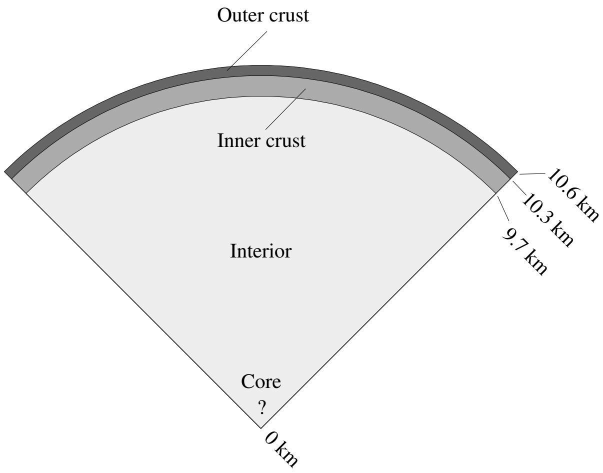

Figure 2.1: A model of a $1.4M_\odot$ neutron star. No atmosphere is shown. See description of the layers in the main text. This figure is taken from [4, page 603].

and the nuclei become neutron-enriched[2]. The envelope extends down to the density of $\sim 4.3 \times 10^{11}$ g/cm^3, where it becomes energetically favorable for the neutrons to "leak" out of the nuclei. This process is referred to as the *neutron drip* [23]. The gas of free neutrons that appears in the star below the neutron drip carries heat efficiently so the star is isothermal below that point.

Immediately below the envelope lies the *inner crust*. This layer is composed of a three-component mixture of a (neutron-rich) nuclear lattice, superfluid neutrons and relativistic electrons. As the density increases, more and more neutrons leak from the nuclei and there are fewer electrons or protons per neutron present. At density $\sim 4 \times 10^{12}$ g/cm^3 the pressure from degenerate neutrons begins to dominate over the electron degeneracy pressure.

The transition from the inner crust to the *interior* occurs where the density reaches nuclear density, $\sim 2 \times 10^{14}$ g/cm^3, where the nuclei finally dissolve.

The physics and composition of matter in the center of neutron stars, where the density may reach and exceed 10^{15} g/cm^3, are still not understood (see e.g. Heiselberg & Pandharipande [10] and Lattimer & Prakash [14] for reviews) and there are no experimental constraints to give guidance in this regime.

In this work we are primarily interested in the thermal structure of neutron stars and we will therefore concentrate on the envelope which we define here as the region

[2]The composition of nuclei in the envelope is further explained in section 3.1.

from the stellar surface to a density of 10^{10} g/cm^3.

2.2 Thermal Structure Equations

Let us now consider the general relativistic equations that govern the the thermal structure of a static, spherically symmetric, non-rotating star of mass M and radius R. In the following we are guided by the discussion of [8], where further references are given.

In Newtonian mechanics we can express the condition of hydrostatic equilibrium, where the pressure gradient just cancels the gravitational attraction, by:

$$\frac{dP}{dr} = -\frac{Gm\rho}{r^2}, \tag{2.1}$$

where $P = P(r)$ is the pressure, G is the gravitational constant, $\rho = \rho(r)$ is the density and $m = m(r)$ is the mass inside a sphere of radius r. However, Newtonian mechanics is inadequate to describe neutron stars. This we can see by calculating the Newtonian escape velocity at the surface of a neutron star of radius $R_{\rm ns} = 15$ km and mass $M_{\rm ns} = 1.4 M_\odot$:

$$v_{\rm esc} = \sqrt{\frac{2GM_{\rm ns}}{R_{\rm ns}}} \approx 0.5c$$

where c is the speed of light. Furthermore, the ratio of the Newtonian gravitational energy to the rest mass energy of a test mass, m, on a neutron star surface is:

$$\frac{GM_{\rm ns}m/R_{\rm ns}}{mc^2} \approx 0.14$$

It is therefore clear that relativistic effects must be considered when discussing neutron star surfaces. In general relativity theory, hydrostatic equilibrium is expressed by the Tolman-Oppenheimer-Volkoff equation:

$$\frac{dP}{dr} = -\frac{Ge^{2\Lambda}}{r^2}\left[m + 4\pi r^3 P/c^2\right]\left[\rho + P/c^2\right] \tag{2.2}$$

where the potential $\Lambda = \Lambda(r)$ takes into account the curvature of space and is given by:

$$e^{\Lambda} = \frac{1}{\sqrt{1 - 2Gm/rc^2}}.$$

An essential difference between Newtonian mechanics and relativity theory is that in the latter case the source of the gravitational field is the energy-momentum tensor and not just the mass density. As a result, both energy and pressure give rise to gravitational fields in very compact objects.

The general relativistic thermal transport equation is given by:

$$\frac{d\left(Te^{\phi/c^2}\right)}{dr} = -\frac{3}{16}\,\frac{\kappa\rho}{T^3}\,\frac{L_\mathrm{d}}{4\pi\sigma r^2}\,e^{\phi/c^2}e^{\Lambda}, \tag{2.3}$$

where $\kappa = \kappa(r)$ is the opacity[3], σ the Stefan-Boltzmann constant, L_d the photon luminosity, (Te^{ϕ/c^2}) the redshifted temperature, and e^{ϕ/c^2} is the gravitational redshift factor, with the gravitational potential, $\phi = \phi(r)$, given by the *source equation*:

$$\frac{d\phi}{dr} = \frac{G\left(m + 4\pi r^3 P/c^2\right)}{r^2(1 - 2Gm/rc^2)} \tag{2.4}$$

Outside the star, where $r > R$, ϕ is given by:

$$e^{\phi/c^2} = \sqrt{1 - \frac{2GM}{rc^2}}.$$

In principle, equations (2.2) and (2.3) can be integrated together to give the star's thermal structure once $m(r)$, $P(r)$ and $\kappa(r)$ are known functions. However, in the next section we will show how the problem can be greatly simplified.

2.3 Neutron Star Envelopes

Following Gudmundsson et al. [7], we divide neutron stars into two regimes: the thermally insulating envelope and the isothermal interior (which refers to the whole star below the envelope). This division is useful since the core holds much more thermal energy and evolves only over a long time scale whereas the envelope holds little mass and has a much shorter thermal relaxation time. Thus, at any given time, the envelope is in a quasi-static thermal equilibrium with the isothermal core.

We define the envelope as the outer layers where the thermal gradient is non-zero. By our definition the envelope starts where Eddington's criteria is met, at

[3]Unfortunately, the notation for opacity seems to vary in the field. In this work we use κ for the opacity, which related to the *thermal conductivity*, λ by: $\kappa = 16\sigma T^3/(3\rho\lambda)$. For more information, see chapter 4.

optical depth of 2/3:

$$P_{\rm s} = \frac{2}{3}\,\frac{g_{\rm s}}{\kappa_{\rm s}}, \tag{2.5}$$

where we have introduced the surface gravity:

$$g_{\rm s} = \frac{GM}{R^2} e^{\Lambda_{\rm s}} \tag{2.6}$$

(which, for neutron stars, is typically $\sim 10^{14}$ cm/s^2) and $\kappa_{\rm s}$ is the surface opacity. The density at which condition (2.5) is met is $\rho_{\rm s} \sim 0.1$–10 g/cm^3, depending on the magnetic field strength and the surface temperature[4]. The envelope ends, and the interior begins, at the depth where the temperature gradient vanishes. We find that this occurs at the density $\rho_{\rm b} \sim 10^{10}$ g/cm^3, well before the neutron drip starts.

2.3.1 Electrons in the Envelope

Since electrons are fermions they must obey the Pauli exclusion principle, which forbids any two fermions to share the same quantum state. In a cold and dense plasma, there are too many particles crowding on too few energy levels. Once the lowest energy levels are filled, the remaining fermions are pushed up to higher energy levels, forming a *degenerate* gas. A fully degenerate gas is one where all the energy levels up to the *Fermi energy* are filled and all of the higher levels are empty.

The electrons in neutron star envelopes can display any degree of degeneracy. This we can see by considering the Fermi temperature of the electrons as a function of density:

$$T_{\rm F} = \frac{1}{k}\left(\epsilon_{\rm F} - m_{\rm e}c^2\right)$$

where k is the Boltzmann constant, $\epsilon_{\rm F} = (m_{\rm e}^2c^4 + p_{\rm F}^2c^2)^{1/2}$ is the Fermi energy, $m_{\rm e}$ is the electron mass, $p_{\rm F} = \hbar(3\pi^2 n_{\rm e})^{1/3}$ is the Fermi momentum and $n_{\rm e} = Z\rho/Am_{\rm p}$ is the number density of electrons, and m_p is the mass of the proton. This leads to the following expression for the Fermi temperature in terms of density:

$$T_{\rm F} = \frac{1}{k}\left(\sqrt{m_{\rm e}^2c^4 + c^2\hbar^2\left[\frac{3\pi^2 Z\rho}{Am_{\rm P}}\right]^{2/3}} - m_{\rm e}c^2\right). \tag{2.7}$$

[4]See also graph 5.1 and section 5.1.

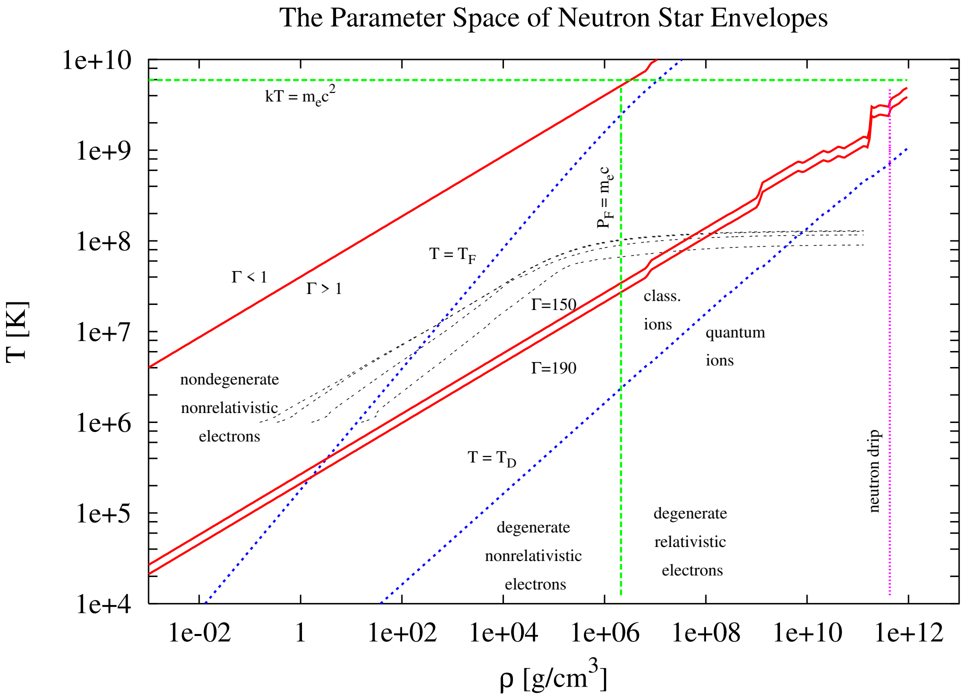

Figure 2.2: The parameter space of interest for the study of neutron star envelopes. The green, dashed horizontal line at the top of the graph shows the temperature at which non-degenerate electrons become relativistic (well above the region of interest in this work) and the green, dashed vertical line in the middle of the graph shows the density at which degenerate electrons become relativistic. The red solid curves show contours of constant Γ (the Coulomb interaction parameter, explained in 3.2.2). $\Gamma_{\rm melt}$ is bound by the two contours marked $\Gamma = 150$ and $\Gamma = 190$. The ions are in liquid phase above that curve, but in solid phase below. The blue, dotted line marked $T = T_{\rm F}$ shows the electron Fermi temperature as a function of density. On the right hand side of this line the electrons are increasingly degenerate. The blue, dotted line marked $T = T_{\rm D}$ shows the Debye temperature as a function of density. To the left and above that line the ions behave classically, but to the right and below, quantum corrections become important. The thin, black, dotted curves represent sample thermal profiles. The purple, dashed, vertical line at the right hand side of the graph shows where the neutron drip occurs.

In figure 2.2 we have plotted, among other curves, the Fermi temperature as a function of density. To the right of that curve the electrons become increasingly degenerate and to the left the electrons behave more or less classically. We can see that the sample thermal profiles extend across the $T_{\rm F}(\rho)$ curve; therefore the electrons in the envelope can be either nod-degenerate or degenerate.

The electrons can become relativistic at high enough temperature or density. Non-degenerate electrons become relativistic when their thermal kinetic energy becomes comparable to their mass energy:

$$kT \sim m_e c^2.$$

This gives us the temperature where non-degenerate electrons become relativistic, $T_{rel} \sim 6 \times 10^9$ K.

Degenerate electrons become relativistic when their Fermi momentum is of the order of $m_e c$. This is condition is met at the density given by

$$\rho_{rel} = \frac{Am_p}{3Z\pi^2}\left(\frac{m_e c}{\hbar}\right)^3 \approx 2 \times 10^6 \mathrm{g/cm}^3.$$

In figure 2.2 we have drawn the straight lines corresponding to these conditions. The electron gas of the envelopes we calculate is never hot enough to host non-degenerate relativistic electrons (as can be seen from the sample thermal profiles). Since the thermal profiles extend across the the $\rho = \rho_{rel}$ the degenerate electrons do become relativistic at that point in the envelope.

2.3.2 Ions in the Envelope

At relatively low temperature and high densities, the ions experience quantum effects due to lattice vibrations. For ions in the minimum-energy configuration of a body-centered-cubic lattice this occurs when the temperature of the envelope is below the *Debye temperature*, given by:

$$T_D = 0.45\,\frac{\hbar}{k}\,\frac{Ze}{Am_p}\,\sqrt{4\pi\rho}.$$

At temperatures lower than T_D, quantum effects have to be taken into account and where $T > T_D$, the ions are classical. Looking again at the thermal profiles in figure 2.2, we see that the ions are strongly coupled only at the higher densities at the bottom of the envelope, where the temperature gradient is zero.

2.4 The Plane-Parallel Approximation

Since neutron star envelopes are a very thin layer (~ 100 m) containing only a tiny portion of the star's mass ($M_{env}/M_{ns} \approx 10^{-7}$), we can safely make a set of useful approximations, known collectively as the *plane-parallel approximation* [8].

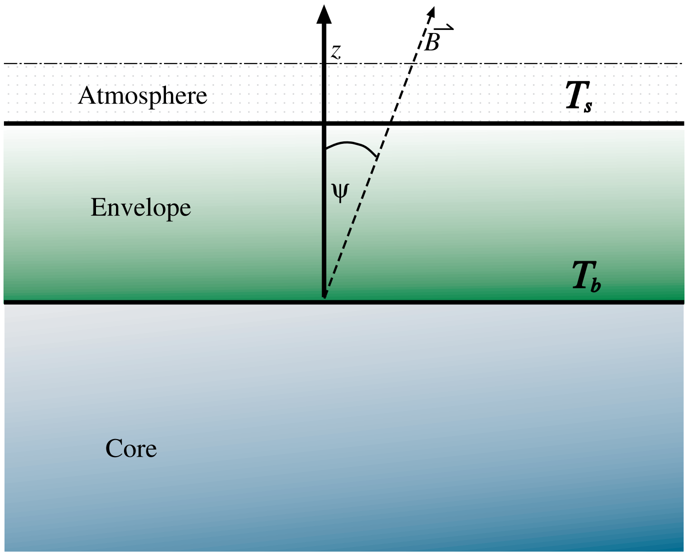

Figure 2.3: Here we explain some quantities in our model of the envelope. $T_{\rm s}$ is the *surface* temperature and $T_{\rm b}$ is the temperature at the *boundary* between the envelope and the core. The surface is defined to be at optical depth $= 2/3$, and the boundary where the temperature gradient vanishes, at $\rho \approx 10^{10}$ g/cm^3.

In this approximation we effectively peel off and flatten the envelope and consider only the thermal structure in the radial direction. Below the envelope lies the core at uniform temperature $T_{\rm b}$. We assume the entire mass of the star lies in the core so that inside the envelope we can replace the $m(r)$ function with the constant value M. Furthermore we can ignore variations in the curvature factor, which are of the order of 0.7% [8], and replace it with its surface value:

$$e^{\Lambda(r)} \approx e^{\Lambda_{\rm s}} = \frac{1}{\sqrt{1 - 2GM_{\rm ns}/R_{\rm ns}c^2}}$$

Similarly, we can replace the gravitational redshift factor with its surface value:

$$e^{\phi(r)/c^2} \approx e^{\phi_{\rm s}/c^2}.$$

Since we now regard e^{ϕ/c^2} as a constant, we can take it outside the differential in equation (2.3) and thus we see that it cancels from the thermal transport equation in the envelope. We can also see that in the envelope,

$$\frac{P/c^2}{\rho} \sim 10^{-3}$$

and therefore the pressure terms in equation (2.2) are negligible and we can dispense with them. Finally, since there is no neutrino emission or other energy sinks in the envelope, it follows from energy conservation that the luminosity, $L_{\rm d}$, is constant throughout the envelope and we can set it to equal its surface value:

$$L_{\rm d} = 4\pi\sigma R_{\rm ns}^2 T_{\rm s}^4.$$

These approximations, taken together, reduce equations (2.2) and (2.3) to:

$$\frac{dP}{dr} = -\frac{GM_{\rm ns}e^{2\Lambda_{\rm s}}\rho}{r^2} \tag{2.8}$$

$$\frac{dT}{dr} = -\frac{3}{16}T_{\rm s}^4 e^{\Lambda_{\rm s}}\left[\frac{R_{\rm ns}}{r}\right]^2\frac{\kappa\rho}{T^3} \tag{2.9}$$

By dividing equation (2.9) by equation (2.8) we get the following *thermal structure equation*:

$$\begin{aligned}\frac{dT}{dP} &= \frac{3}{16}\frac{T_{\rm s}^4 R_{\rm ns}^2}{GM_{\rm ns}e^{\Lambda_{\rm s}}}\frac{\kappa}{T^3} \\ &= \frac{3}{16}\frac{T_{\rm s}^4}{g_{\rm s}}\frac{\kappa}{T^3}\end{aligned} \tag{2.10}$$

where, in the latter expression, we have inserted the expression for the surface gravity from equation (2.6). We note that in deriving this equation the largest error introduced is of the order of $\lesssim 1\%$ [8]. Studying the above equation, we see that, given the physical input in the form of κ and P, the thermal structure of neutron star envelopes depends only on the ratio

$$\mathcal{E} \equiv T_{\rm s}^4/g_{\rm s}, \tag{2.11}$$

which is called *the Eddington number*. This result, first realized by Gudmundsson et al. [8], greatly simplifies our envelope models since three parameters, $T_{\rm s}$, $R_{\rm ns}$, and $M_{\rm ns}$, have been combined into one. The resulting thermal structure equation is now simply:

$$\frac{dT}{dP} = \frac{3}{16}\,\mathcal{E}\,\frac{\kappa}{T^3} \tag{2.12}$$

Equation (2.12) can be integrated to give the thermal structure, given that the

equation of state and the opacity are known. However, in this work we choose to integrate a different, but equivalent set of equations derived below.
We can rewrite equation (2.8) as

$$\frac{dP}{dr} = g_{\mathrm{s}} e^{\Lambda_{\mathrm{s}}} \left[\frac{R}{r}\right]^2 \rho \tag{2.13}$$

We note the occurrence of the factor $e^{\Lambda_{\mathrm{s}}}(R/r)^2$ in the right hand side of both equations (2.13) and (2.9). We can hide this factor by introducing a new depth coordinate, z, defined as:

$$z \equiv -\int_R^r \left[\frac{R}{r'}\right]^2 e^{\Lambda_{\mathrm{s}}} dr' \tag{2.14}$$

Integrating, we find an expression for z:

$$\begin{aligned} z &= e^{\Lambda_{\mathrm{s}}} R^2 \left(\frac{1}{r} - \frac{1}{R}\right) \\ &= e^{\Lambda_{\mathrm{s}}} R \left(\frac{R-r}{r}\right). \end{aligned}$$

Inserting $x = R - r$ and $r = R - x$, where x is the actual depth we get:

$$\begin{aligned} z &= e^{\Lambda_{\mathrm{s}}} x \frac{R}{R-x} \\ &= e^{\Lambda_{\mathrm{s}}} x \left(1 - \frac{x}{R}\right)^{-1} \end{aligned}$$

In terms of the new coordinate, equations (2.9) and (2.8) above become simply:

$$\frac{dP}{dz} = g_{\mathrm{s}} \ \rho \tag{2.15}$$

and

$$\frac{dT}{dz} = \frac{3}{16} T_{\mathrm{s}}^4 \ \frac{\rho\kappa}{T^3}. \tag{2.16}$$

Instead of integrating this set of equations (equations (2.15) and (2.16)) we find it more convenient for our purposes to integrate the density gradient. To find it, we expand the pressure gradient as:

$$\frac{dP}{dz} = \left(\frac{\partial P}{\partial \rho}\right)_T \frac{d\rho}{dz} + \left(\frac{\partial P}{\partial T}\right)_\rho \frac{dT}{dz}$$

and solve for the density gradient:

$$\frac{d\rho}{dz} = \left[\frac{dP}{dz} - \left(\frac{\partial P}{\partial T}\right)_\rho \frac{dT}{dz}\right] \frac{1}{(\partial P/\partial \rho)_T}.$$

After inserting the expressions for the pressure gradient from equation (2.15) and the temperature gradient from equation (2.16) we get:

$$\frac{d\rho}{dz} = \frac{g_s \rho}{(\partial P/\partial \rho)_T} \left[1 - \left(\frac{\partial P}{\partial T}\right)_\rho \frac{3}{16} \frac{T_s^4}{g_s} \frac{\kappa}{T^3}\right] \tag{2.17}$$

this, along with the temperature gradient, in the form of equation (2.16), are the actual equations which we integrate in our code.

We will discuss the physical input used in this work in the next two chapters and describe the details of our numerical calculations in chapter 5.

Chapter 3

The Equation of State of Highly Magnetized Envelopes

We now turn our attention to the physical input needed to integrate equations (2.17) and (2.16) through neutron star envelopes. In this chapter we consider the parameter space, discuss the pressure in the envelope and describe the method we use to calculate our equation of state. We begin with a discussion on the envelope's chemical composition.

3.1 The Composition of the Envelope

In our model, the plasma in the envelope consists of fully ionized nuclei immersed in a neutralizing background of electrons.

We neglect the possible effects of partially ionized layers since electron energy levels in the strong magnetic field are very difficult to compute. Since a strong magnetic field will raise the binding energy of atoms, it also shifts the ionization equilibrium, lowering the degree of ionization. Therefore plasma which would be fully ionized at some ρ and T in the absence of a magnetic field might be only partially ionized in a strong magnetic field. Fortunately, we will see that the T_{b}–T_{s} relationship for reasonably hot neutron stars is not noticeably changed if the conditions in the outermost layers are perturbed[1]. We therefore base our equation of state on a fully ionized plasma.

In this work we further assume that the neutron star has not accreted lighter

[1] See also the results of Potekhin et al. [20].

nuclei from the interstellar medium or a companion star[2] therefore, at the lowest densities at the top of the envelope, the nuclei present are assumed to be ^{56}Fe. Less massive nuclei have a higher proportion of their nucleons at the surface where they are less bound, making the nucleus less stable. For more massive nuclei, the Coulomb repulsion between protons tends to make the nucleus less tightly bound. The balance, with the most bound nuclei, is found with ^{56}Fe.

In the presence of degenerate, relativistic electrons, this equilibrium balance is shifted. The electrons are then energetic enough to induce inverse beta decay:

$$e^- + p^+ \rightarrow n + \nu_e. \tag{3.1}$$

The neutrons tend to decay again into protons and electrons:

$$n \rightarrow p^+ + e^- + \overline{\nu_e} \tag{3.2}$$

at the same rate so the number of protons, electrons and neutrons stays constant. Deep in the envelope, as the nuclei become more and more densely packed, the electron background gets increasingly uniform and degenerate. As the density exceeds $\sim 6 \times 10^6$ g/cm^3, most of the electron energy levels below the Fermi energy have become filled. This restricts the neutron decay process (3.2), as electrons cannot be created in those energy levels that are already filled. Therefore, the nuclei get increasingly neutron-rich. Just below the bottom of the envelope, at density $\sim 4.3 \times 10^{11}$ g/cm^3, the neutron-rich nuclei are pressed together so tightly that they perturb each other's surface tension and the neutron drip occurs. As mentioned before, the free neutrons that appear at these high densities carry heat efficiently and therefore no thermal gradient is expected below that point. In our calculations we find that the thermal gradient vanishes, i.e. the thermal profile flattens out, at the bottom of the envelope, at densities well below the neutron drip. Hence, the assertion that the the thermal gradient is non-zero only in the envelope in neutron stars is justified.

The neutronization of equilibrium nuclei is described by Baym et al. [1] and tables relating the density and the dominant species of nucleus for cold catalysed matter (hereafter referred to as BPS-composition or BPS-matter) are given. In our models of the envelope we use their results for the composition. In figure 3.1 we show the

[2]See Chabrier et al. [5] and Potekhin et al. [19] for a discussion of the effects of accretion.

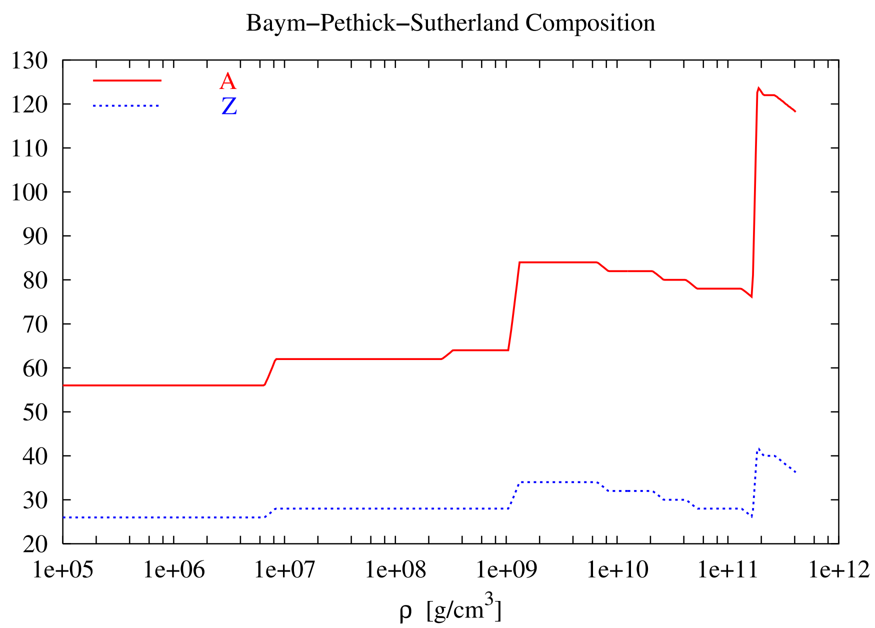

Figure 3.1: The composition of BPS-matter as calculated by Baym et al. [1]. The curves show how the mass number, A, and the atomic number, Z, of equilibrium nuclei depends on density. At the lowest density we have assumed the composition to be ^{56}Fe ($Z = 26$ and $A = 56$). In our calculations we employ a simple linear interpolation between the tabulated values given in[1].

variance of the nuclear charge and mass number with density in BPS-matter. Since the equilibrium nuclei depend only on nuclear reactions, the neutron star magnetic fields are not expected to affect the composition of their envelopes.

3.2 The Pressure in the Envelope

The pressure in the envelope is a sum of the matter pressure (which stems from ions and electrons) and radiation pressure (from photons).

We will discuss each pressure term individually in the following subsections and then give a few, selected samples of our equation of state at the end of this chapter. No attempt is made to display our equation of state fully in this chapter, but rather we focus on representative samples. More extensive plots of the pressure are presented in appendix A.

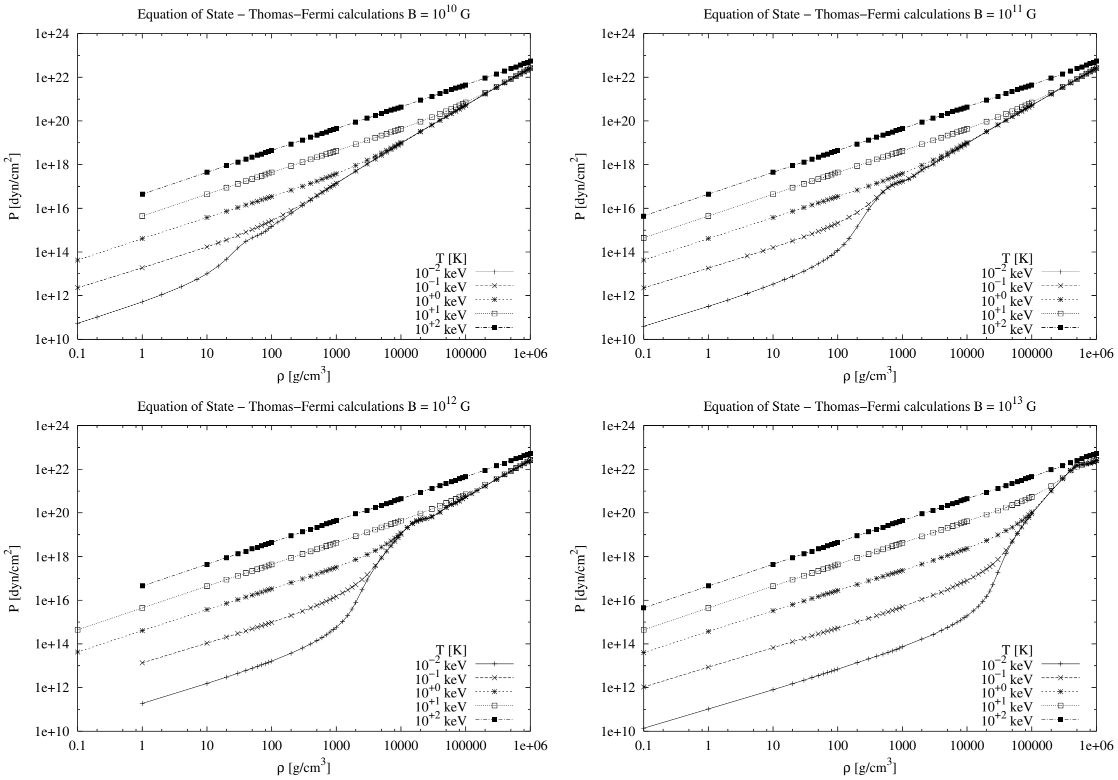

Figure 3.2: Electron pressure in the Thomas-Fermi approximation as computed by Thorolfsson et al. (1998) plotted as a function of density (see Thorolfsson et al. [26] and Rögnvalsson et al. [22] for details). Each panel shows the electron pressure at a fixed magnetic field strength, $B = 10^{10}$, 10^{11}, 10^{12} and 10^{13} [G]. These figures represent the entire data set published on the Internet. Note that the Thomas-Fermi pressure is only offered at five values for the temperature ($T = 10^{-2}, 10^{-1}, 10^{0}, 10^{1}$ and 10^{2} keV, where 1 keV $= 1.160445 \times 10^{7}$ K). Note also that at a high enough density the curves converge and the pressure becomes almost independent of temperature. The "humps" of the low temperature curves correspond to the Landau levels.

3.2.1 Electron Pressure

At low densities in the envelope, we use the pressure calculated in the Thomas-Fermi approximation by Thorolfsson et al. [26] and Rögnvaldsson et al. [22]. In these calculations, all Landau levels have been taken into account and finite temperature effects are included. The resulting pressure tables are available via the Internet[3]. We plot their results in figure 3.2. Note that the points have been densely given as a function of density, but only sparsely given for five values of temperature ($T \approx 1.16 \times 10^{5}, 1.16 \times 10^{6}, 1.16 \times 10^{7}, 1.16 \times 10^{8}$ and 1.16×10^{9} K). This led to the largest contribution of uncertainties in our equation of state and by adding more points for other temperatures our equation of state could have been improved, although, due

[3] The data can be found at `http://www.raunvis.hi.is/~ath/TFBT/`

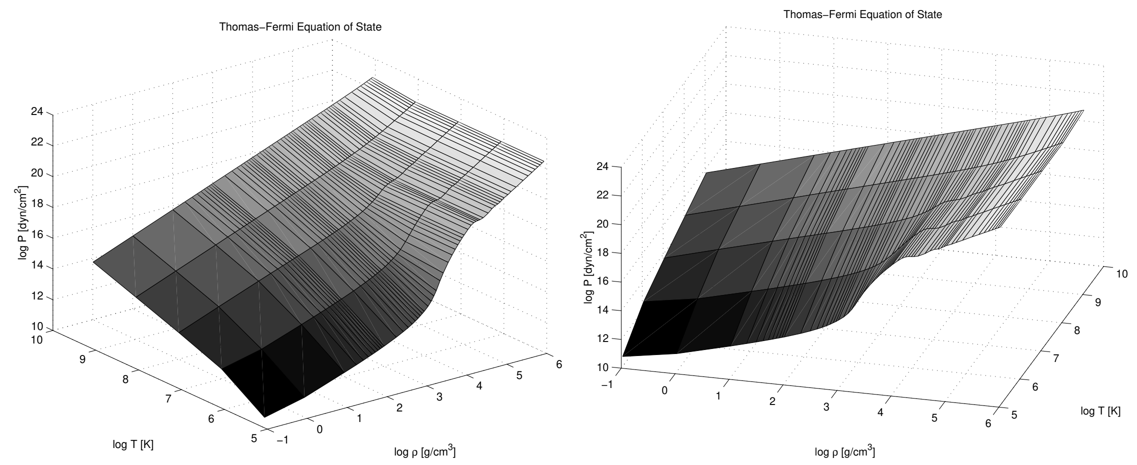

Figure 3.3: The Thomas-Fermi pressure surface. Shown here are two separate views of the same $P_{\text{T-F}}(\rho, T)$ surface in the case where $B = 10^{12}$ G.

to time constraints we do not attempt this here. We will show in section 6.1 that this limitation will have only a minor effect on our results.

As the density increases, the nuclei are squeezed closer to each other, the electron distribution becomes increasingly homogeneous and quantum effects come into play. In this zone, the Thomas-Fermi approximation approaches that of a free electron gas, and as the electrons get more and more relativistic, the effects of the magnetic field diminish. The electron pressure can then be calculated by evaluating the appropriate Fermi-Dirac integrals. Eggleton et al. [6] have devised a simple calculation method that approximates the Fermi-Dirac integrals to a quoted accuracy of 0.1%. We implement their method in our code, but add a lattice correction term (described below) and use the result for our electron pressure at densities $\rho \gtrsim 10^6$ g/cm^3.

The final electron pressure is then formed by fusing together these two zones manually to assure a smooth transition from one to the other. We show a sample of the resulting combined profiles in figure 3.4.

3.2.2 Ion Pressure

A detailed description of the physics of ions in non-magnetic envelopes can be found in Gudmundsson [9, Pages 65-68, 75-80] and Gudmundsson et al. [8, Section III]. Since the ions are too massive to be strongly affected by the magnetic field, the discussion there applies to magnetic envelopes. The following description is based on theirs and we direct the interested reader to the aforementioned articles and to

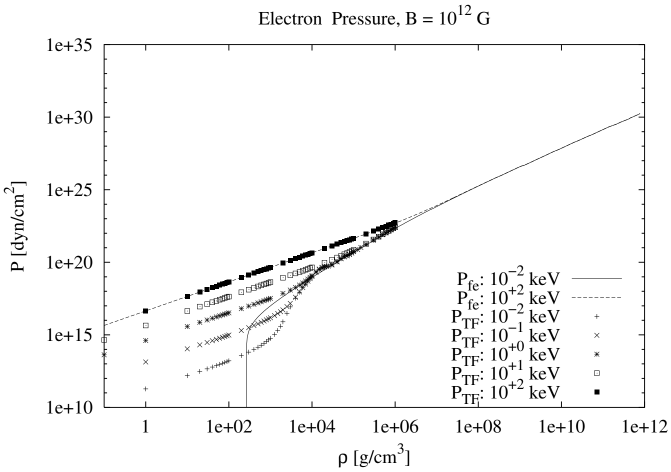

Figure 3.4: Electron pressure in the case where $B = 10^{12}$ G. The points correspond to the Thomas-Fermi pressure and the solid and dashed curves correspond to the free-electron pressure at the highest (dashed) and lowest (solid) temperatures, as computed by our code using Eggleton's method. Included in the free-electron pressure is the Coulomb correction term for ion-ion interaction (see subsection 3.2.2 for explanation). Note that at low temperature (solid curve) the free electron pressure in Eggleton's approximation falls to zero. Note also how the curves converge at around $10^6 - 10^7$ g/cm^3.

the references therein for more information.

In contrast to the free electrons, the massive ions remain non-relativistic throughout the envelope and are strongly affected by ion-ion Coulomb perturbations even at relatively low densities and high temperatures. To evaluate the ion pressure term we calculate the ideal gas pressure of the ions, $P_{\rm i} = n_{\rm i}kT$, and add to it the ion-ion Coulomb perturbation term $P_{\rm C}$. We note that in the Thomas-Fermi calculations of the electron pressure, this correction is already taken into account. This is because the Thomas-Fermi method calculates the pressure at the boundary of adjacent Wigner-Seitz cells and each cell sees every other cell as a neutral (ions+electrons) "body". Therefore, we only need to add $P_{\rm C}$ to the equation of state where Eggleton's free-electron method was implemented.

To calculate the correction term, $P_{\rm C}$, we introduce the dimensionless *Coulomb interaction parameter* Γ as:

$$\Gamma = \frac{(Ze)^2}{kTr_{\rm i}}$$

where $r_{\rm i}$ is the radius of a single-ion sphere:

$$r_{\rm i} = \left(\frac{4\pi}{3}n_{\rm i}\right)^{-1/3} = \left(\frac{4\pi}{3}\frac{\rho}{Am_{\rm p}}\right)^{-1/3}$$

and $n_{\rm i} = \rho/(Am_{\rm P})$ is the ion number density. We can rewrite Γ in terms of the temperature and density as:

$$\Gamma(T,\rho) = \frac{(Ze)^2}{kT}\left(\frac{4\pi\rho}{3Am_{\rm p}}\right)^{1/3}$$

Γ is a measure of the interaction between the ions. At very low densities and high temperatures, Γ is small and the ions form a classical, ideal gas. When Γ is large the ions become strongly perturbed by Coulomb interactions. In figure 2.2 in the previous chapter, we show the $\Gamma(\rho) = 1$ contour for BPS-matter. On the left hand side of that curve, the ions are weakly coupled whereas on the right side Coulomb corrections become important. A quick look at the thermal profiles in that figure confirms that the ions are strongly coupled throughout the envelope.

At a critical value of $\Gamma = \Gamma_{\rm melt}$, the ions shift phase from liquid ($\Gamma < \Gamma_{\rm melt}$) to solid ($\Gamma > \Gamma_{\rm melt}$). Calculating the precise value of $\Gamma_{\rm melt}$ is a difficult physical problem and one which has not been completely solved yet. In our calculations we set $\Gamma_{\rm melt} = 170$. In figure 2.2 we have drawn two curves representing $\Gamma_{\rm melt} = 150$ and $\Gamma_{\rm melt} = 190$ to show the range of plausible values for $\Gamma_{\rm melt}$. We find that the final equation of state is not sensitive to the exact value of $\Gamma_{\rm melt}$.

We take the ion-ion Coulomb interaction into account by adding to the ideal ion gas pressure, $P_{\rm i}$,:

$$P_{\rm i} = \frac{kT}{Am_{\rm p}}\,\rho,$$

a correction term, $P_{\rm C}$:

$$P_{\rm C} = \frac{1}{3}F(\Gamma)P_{\rm i}, \tag{3.3}$$

where A is the mass number of the envelope nuclei (BPS-matter in our case) and F is a function of Γ given by[4]:

$$F(\Gamma) = \begin{cases} \Gamma^{3/2}\left[\frac{a_1}{(b_1+\Gamma)^{1/2}} + \frac{a_2}{(b_2+\Gamma)} + \frac{a_3}{(b_3+\Gamma)^{3/2}} + \frac{a_4}{(b_4+\Gamma)^2}\right] & \Gamma \le \Gamma_{\rm melt} \\ a_1\Gamma + c_1 + \frac{c_2}{\Gamma^2} & \Gamma > \Gamma_{\rm melt} \end{cases} \tag{3.4}$$

where the constants are given empirically by: $a_1 = -0.895929, a_2 = 0.11340656$, $a_3 = -0.90872827$, $a_4 = -0.11614773$, $b_1 = 4.6664860$, $b_2 = 13.675411$, $b_3 = 1.8905603$, $b_4 =$

[4]See formula (IV.42) in [9].

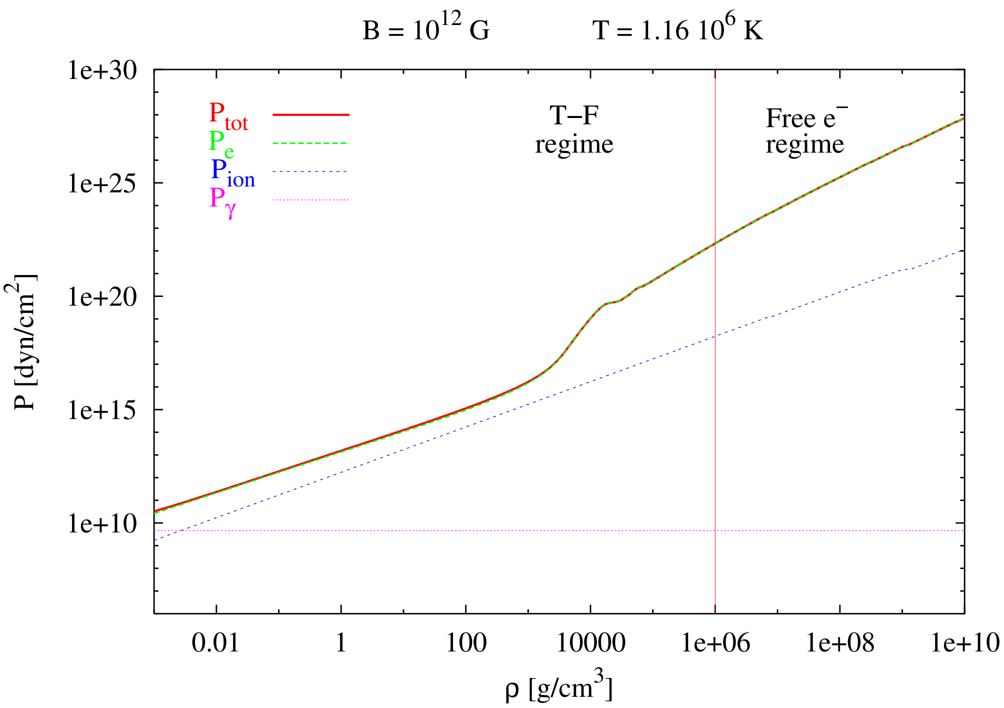

Figure 3.5: The pressure terms as functions of ρ in the case where $B = 10^{12}$ G and $T = 0.1$ keV $\approx 1.16 \times 10^6$.

1.0277554, $c_1 = 1.5$ and $c_2 = 3500$.

For $\Gamma \ll 1$, F reduces to the results of Debye-Hückel theory, $F(\Gamma) \approx -\frac{\sqrt{3}}{2}\Gamma^{3/2}$, and for $\Gamma \gg 1$ F reduces to the Wigner-Seitz result: $F(\Gamma) \approx -\frac{9}{10}\Gamma$.

3.2.3 Photon Pressure

Given the temperature, T, the radiation pressure, P_γ, can easily be calculated as:

$$P_\gamma = \frac{4}{3}\frac{\sigma}{c}T^4$$

This term is only significant in the very low density and mid- to high temperature regime. As we will see, these conditions do not normally occur in neutron star envelopes. We nevertheless retain this term for completeness.

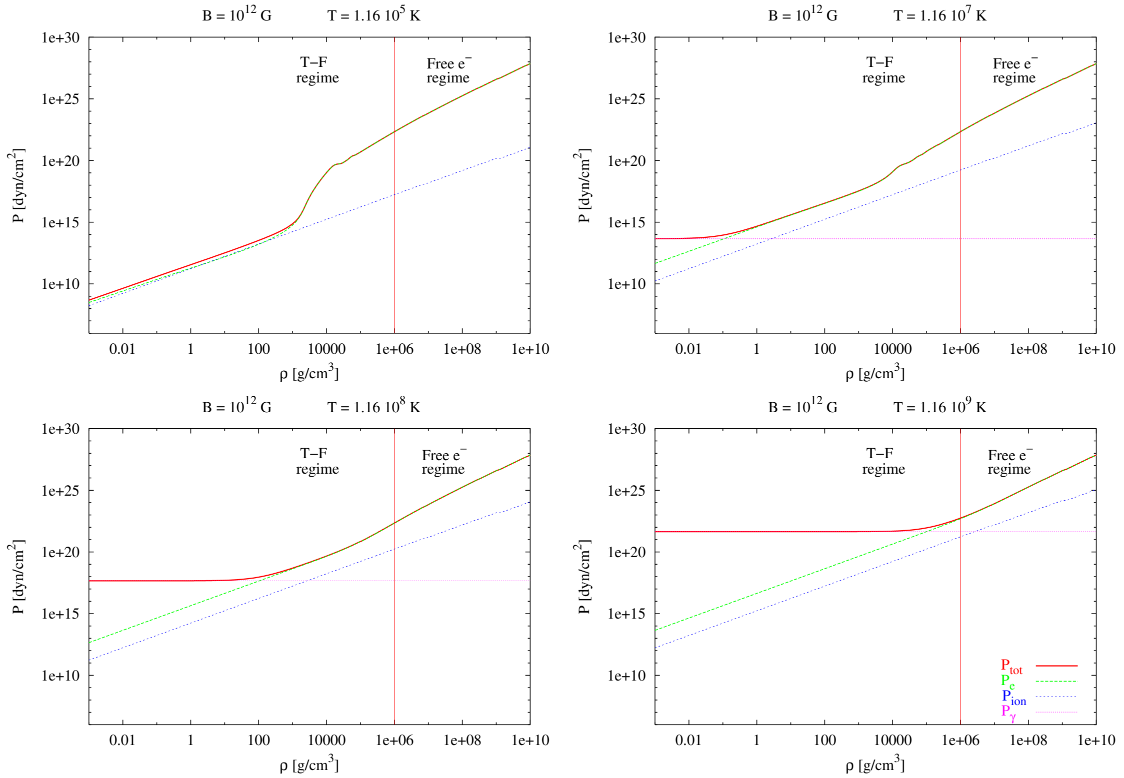

Figure 3.6: The pressure terms in the cases where $B = 10^{12}$ G (same as in figure 3.5). Each panel shows the pressure terms as a function of density for a fixed temperature. (1.16×10^7 K ≈ 1 keV). The labelling is the same as in figure 3.5. The term labelled P_e represents the fused curve consisting of the Thomas-Fermi pressure at lower densities and sum of the free electron pressure plus the Coulomb correction at higher densities.

3.3 The Total Pressure

Keeping the above considerations in mind, we construct our final equation of state by fusing together the pressure over two zones. The following table shows what terms form the total pressure in each zone.

ρ [g/cm^3]	P_tot
$\lesssim 10^6$	$P_\text{T-F} + P_\mathrm{i} + P_\gamma$
$\gtrsim 10^6$	$P_\mathrm{Egg} + P_\mathrm{C} + P_\mathrm{i} + P_\gamma$

Here, the terms in the outer zone correspond to Thomas-Fermi electron pressure, ideal gas pressure of ions and radiation pressure, respectively. The terms in the inner zone correspond to the Eggleton approximation of electron pressure, the ideal gas pressure of ions, the Coulomb correction term and the radiation pressure, respectively.

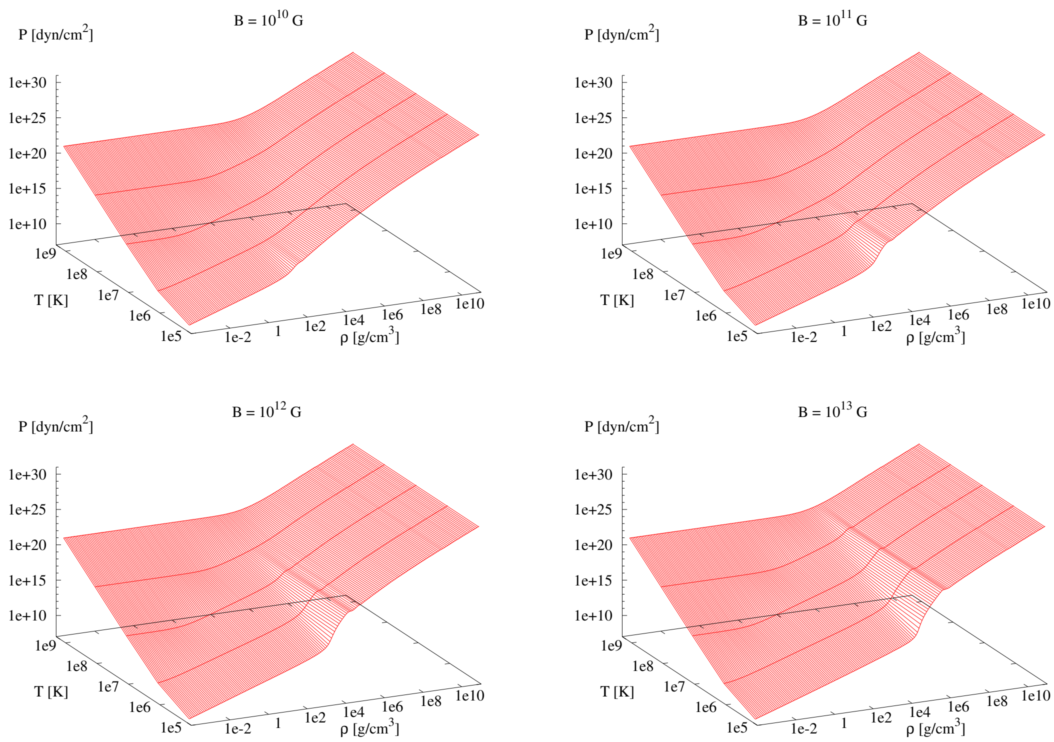

Figure 3.7: The final equation of state shown as surfaces in (ρ, T, P) space. Each panel shows the equation of state for a given magnetic field strength; $B = 10^{10}, 10^{11}, 10^{12}$ or 10^{13} G. All the graphs are drawn in the same scale for easier comparison. We can see in the low density, high temperature corner a flat ramp where the radiation pressure dominates. The sloping flatness in the high density region of the graph shows where the electron pressure dominates.

In figure 3.5, we plot the total pressure along with all the pressure terms on a single graph for comparison. Shown is the case where $B = 10^{12}$ G and $T = 0.1$ keV. In figure 3.6 we show corresponding curves for the other values of T. From this figure (and others presented in appendix A) we see that at the higher densities the electron pressure always dominates. At low densities, the ion pressure becomes increasingly important, except in the hottest case where the radiation pressure overtakes it. This can also be inferred from viewing figure 3.7 where we have plotted the total pressure as a function of temperature and pressure. Each panel in that figure shows the equation of state for a given magnetic field.

In figure 3.8 we show a direct comparison between the surfaces in the highest and lowest magnetic field cases. In the center of that image we see the outlines of an elongated zone, which shows clearly where the effects of the magnetic field are the greatest.

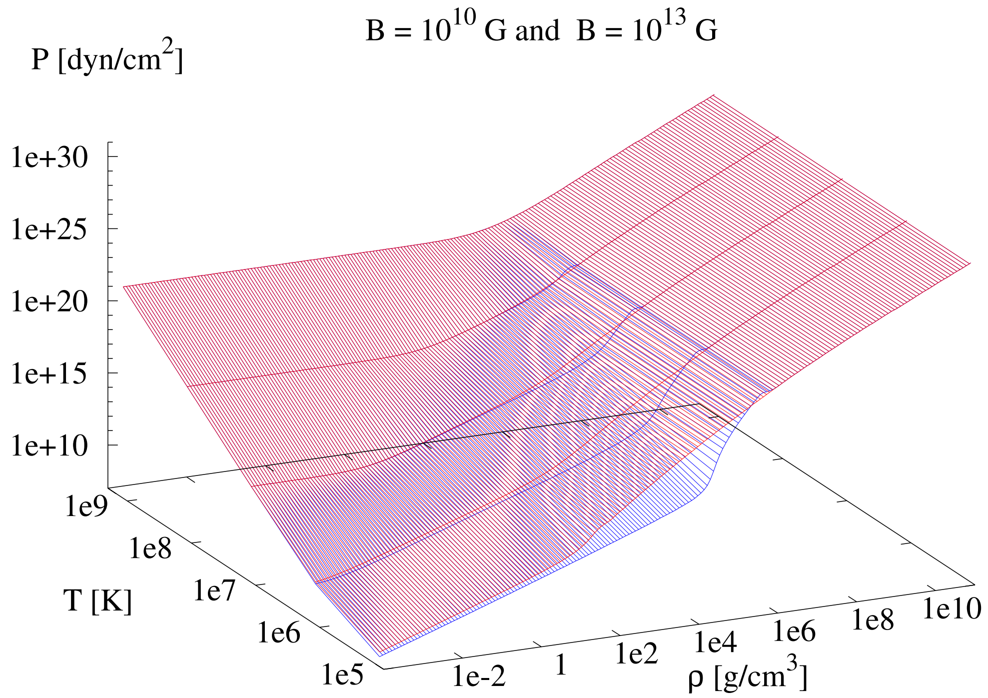

Figure 3.8: Comparison of the equation of state in the cases where the magnetic field is $B = 10^{13}$ G (lower surface) and where $B = 10^{10}$ G (upper surface). At low temperatures and mid-range densities there are clear outlines of the region where the magnetic effects harden the equation of state.

Chapter 4

The Opacity of Highly Magnetized Envelopes

In this chapter we describe the opacity, κ, used in our calculations. We discuss the physical significance of each contribution to the opacity and the methods used to calculate them. Here, we will present only a few sample graphs, but in appendix B we present the opacity in more detail.

4.1 The Sources of Opacity

Neutron stars are born extremely hot and then gradually cool down. The thermal conductivity of their envelopes strongly affects many of their processes in as well as their evolution. For example, the opacity affects the thermal structure, the evolution of the magnetic field and the cooling rate of the star [18]. Unfortunately, the thermal conductivity in the presence of the intense magnetic fields commonly found in neutron stars is extremely difficult to calculate. Therefore, only rough approximating expressions are available.

Thermal transport in neutron star envelopes takes place by a combination of electron conduction and radiative diffusion. In general, these processes occur in parallel and therefore the total opacity is given by:

$$\frac{1}{\kappa_{\rm tot}} = \frac{1}{\kappa_{\rm rad}} + \frac{1}{\kappa_{\rm con}}.$$

Here, $\kappa_{\rm rad}$ is the radiative opacity and $\kappa_{\rm con}$ is the opacity due to electron conduction which is related to the thermal conductivity, λ_c, by

$$\kappa_{\rm con} = \frac{16}{3}\frac{\sigma T^3}{\rho \lambda_{\rm c}}.$$

Typically, radiative diffusion dominates ($\kappa_{\rm rad} \ll \kappa_{\rm con}$ and $\kappa_{\rm tot} \approx \kappa_{\rm rad}$) the thermal transport in the outermost, non-degenerate layers of a neutron star, whereas electron conduction dominates ($\kappa_{\rm con} \ll \kappa_{\rm rad}$ and $\kappa_{\rm tot} \approx \kappa_{\rm con}$) in the deeper, degenerate layers.

Both of these processes are affected by the presence of a strong magnetic field. The mean free path of a photon across the magnetic field is shorter than that of a photon travelling along the magnetic field and therefore the corresponding opacities differ. The field also restricts the motion of the electrons perpendicular to the field to the Landau levels. Thus, the magnetic field effectively introduces anisotropy to the thermal transport, making transport perpendicular to the field more restricted than along it. We therefore need to calculate separately the opacity terms across and along the magnetic field. In the case of a magnetic field at an arbitrary angle ψ to the vertical (cf. fig. 2.3) we have, to a good approximation [27]:

$$\frac{1}{\kappa(\psi)} = \frac{1}{\kappa_{||}}\cos^2\psi \;+\; \frac{1}{\kappa_{\perp}}\sin^2\psi, \tag{4.1}$$

where $\kappa_{||}$ is the longitudinal opacity and $\kappa_{\perp}$ is the transverse opacity.

4.2 Radiative Opacity

The sources of the radiative opacity are Thomson scattering, bound-bound (B-B), bound-free (B-F) and free-free (F-F) absorption.

Calculating the B-B (atomic excitation) and B-F (atomic ionization) contributions in the presence of a strong magnetic field requires knowledge of the electron energy levels and the deformation of heavy atoms in such a field. No accurate theoretical calculations for matter at these conditions exist yet and, since these fields lie beyond the reach of any experimental setup, neither have any empirical constraints been found. We therefore cannot include contributions to the radiative opacity from B-B or B-F absorption. This means that we effectively assume (as we do for the equation of state) the envelope to consist of fully ionized nuclei in a sea of free electrons. This may lead to a serious underestimation of the radiative opacities in the outermost layers by a factor of up to ~ 100 (A. Potekhin 2000, private communica-

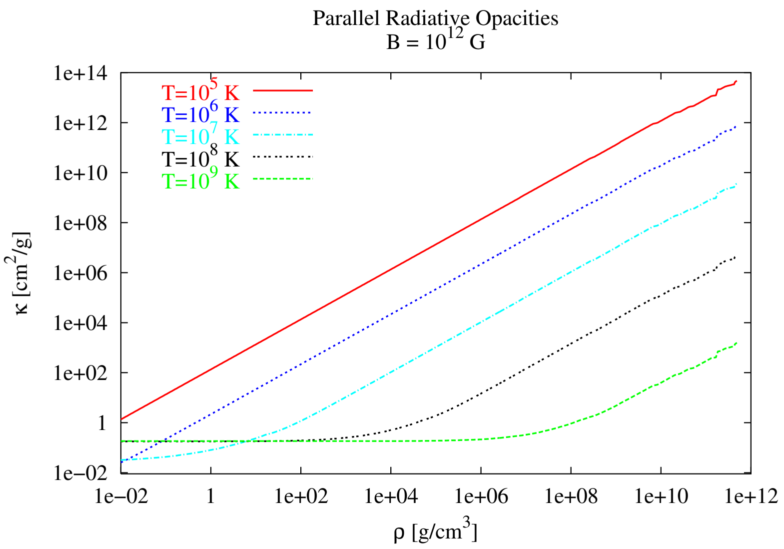

Figure 4.1: Parallel radiative opacities in the case where $B = 10^{12}$ G. Here, $\alpha = 1$.

tion).

Thomson scattering (the scattering of photons by free electrons) and free-free absorption (the absorption of photons by free electrons in the presence of ions) in the strongly magnetic case have been calculated numerically by Shilantev & Yakovlev [24]. Their method relies on the Born approximation, which neglects the motion of the relatively slow, massive ions. This approximation may lead to a further underestimation of $\kappa_{\rm rad}$ by a factor ~ 3 (A. Potekhin 2000, private communication).

We implement Shilantev and Yakovlev's data tables and formulas in our code. Sample plots of the resulting $\kappa_{\rm rad}$ in the case where $B = 10^{12}$ G can be seen in figures 4.1 (parallel case), and 4.2 (orthogonal case). A comparison between the parallel and orthogonal cases can be seen in 4.3.

In an attempt to compensate for the underestimate (due to both the Born approximation and the neglect of B-B and B-F absorption) of $\kappa_{\rm rad}$ we multiply the result by a parameter, α, which we vary from 1 to 300. In general, one would expect α to be a function of density, and be most relevant at the lower densities, where partial ionization may occur, but for the sake of simplicity we take α as constant. We show the effects of α on the total opacity in section 4.4.

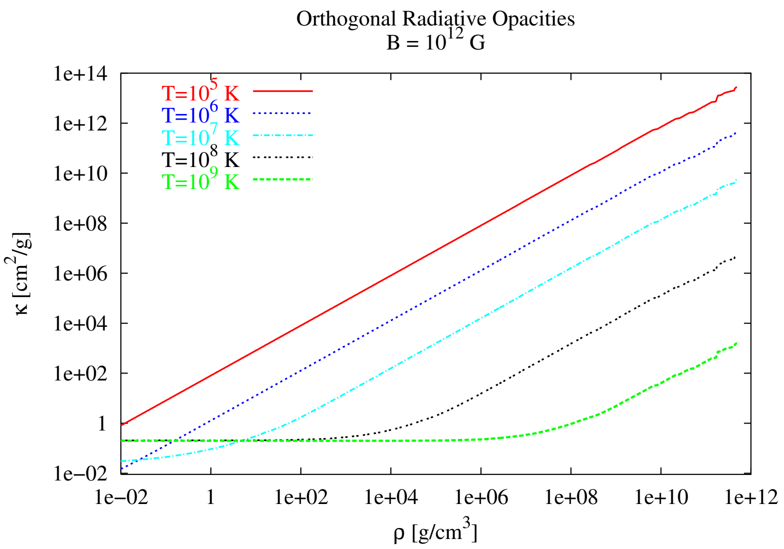

Figure 4.2: Orthogonal radiative opacities in the case where $B = 10^{12}$ G. Here, $\alpha = 1$.

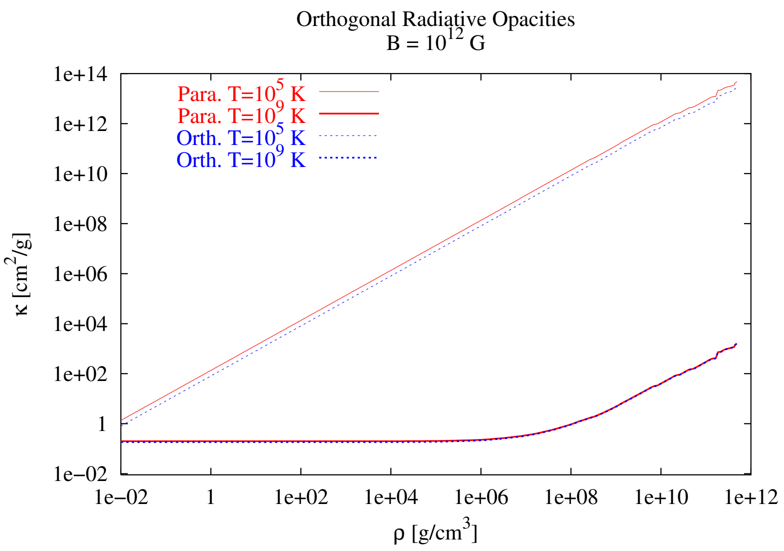

Figure 4.3: Radiative opacities in the cases where $B = 10^{12}$ G. The opacities are plotted for both the parallel and the orthogonal cases and for two values of the temperature, $T = 10^5$ K and $T = 10^9$ K. The difference between $\kappa_{\parallel}$ and $\kappa_{\perp}$ can be seen to be small and decreasing with temperature. Here, $\alpha = 1$.

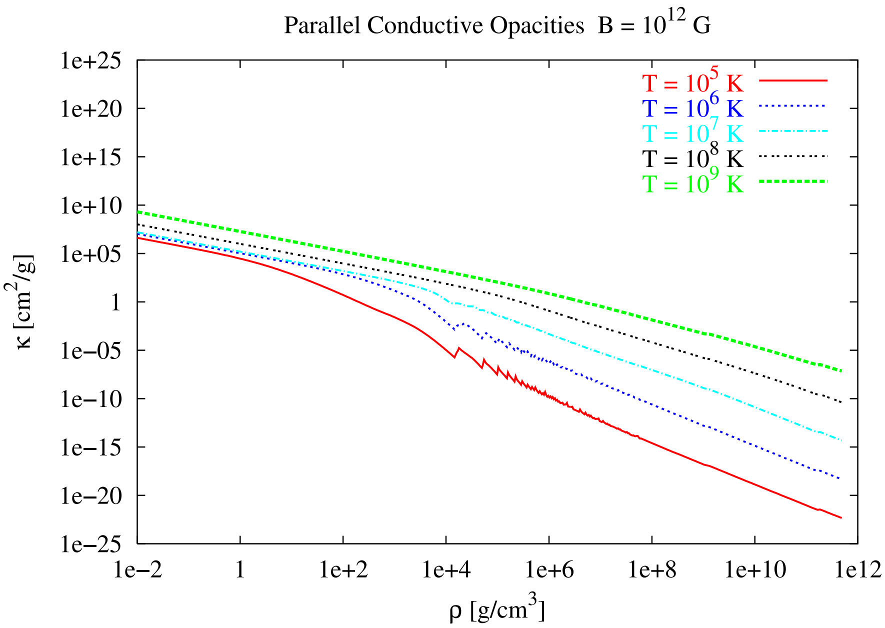

Figure 4.4: The conductive opacity, $\kappa_{\rm con}$ in the parallel case where $B = 10^{12}$ G as calculated by Potekhin's code.

4.3 Conductive Opacity

Heat transport by electron conduction is dominant at high densities. The processes that contribute to $\kappa_{\rm con}$ are electron-phonon, electron-impurity, and electron-electron scattering when the matter is solid and electron-ion and electron-electron scattering when the matter is liquid [8]. The dominant process of electron thermal conduction in neutron star envelopes is electron scattering by correlated ions [18].

The magnetic field affects thermodynamic and kinetic properties of the dense plasma in various ways, depending on density, temperature and field strength. For high enough temperatures the field is *non-quantizing* (classical). Such a field does not affect the thermodynamic properties of matter, but hampers transverse transport and causes Hall currents. In a *weakly quantizing* field the electrons occupy many Landau levels and the thermodynamic functions and kinetic coefficients oscillate with increasing density around their classical values. A *strongly quantizing* magnetic fields confines most electrons to the lowest Landau level. In this case thermodynamic and kinetic properties of matter are very different from those in the classical regime.

We used electron conductivities calculated by a code recently written by A.

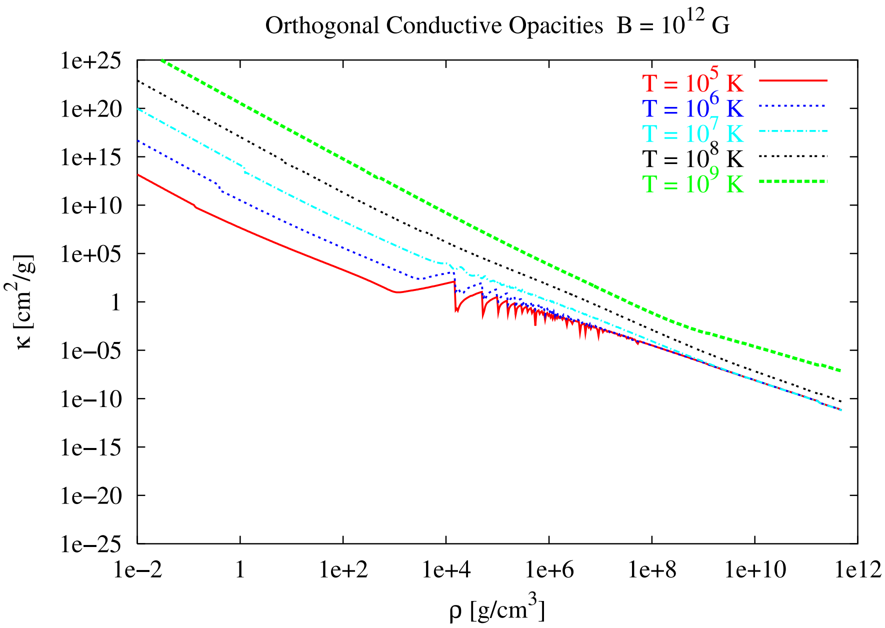

Figure 4.5: The conductive opacity, $\kappa_{\rm con}$ in the **orthogonal** case where $B = 10^{12}$ G as calculated by Potekhin's code.

Potekhin[1]. Details of the method implemented in the code are outside the scope of this work, but can be found in [18]. In short, the thermal conductivity is found using the Wiedemann-Franz law but taking collisions of electrons with ions into account.

Sample results from his code are plotted in figures 4.4 (parallel case), 4.5 (orthogonal case), and 4.6 (comparison).

4.4 The Total Opacity

The total opacity used in this work is determined by:

$$\frac{1}{\kappa_{\rm tot}} = \frac{1}{\alpha\ \kappa_{\rm SY}} + \frac{1}{\kappa_{\rm AP}} \tag{4.2}$$

or

$$\kappa_{\rm tot} = \frac{\alpha\ \kappa_{\rm SY}\ \kappa_{\rm AP}}{\alpha\ \kappa_{\rm SY}\ +\ \kappa_{\rm AP}} \tag{4.3}$$

[1]The code, along with a description of it by its author, is available online at `http://www.ioffe.rssi.ru/astro/conduct/condmag.html`.

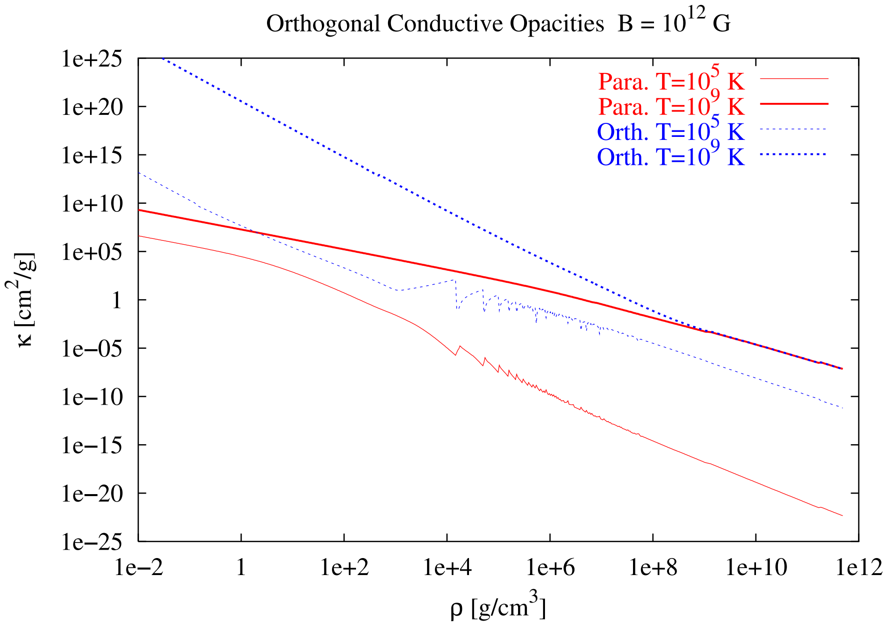

Figure 4.6: For comparison, we show here both the parallel and the orthogonal cases for conductive opacity in the case of the highest and the lowest temperatures in figures 4.4 and 4.5.

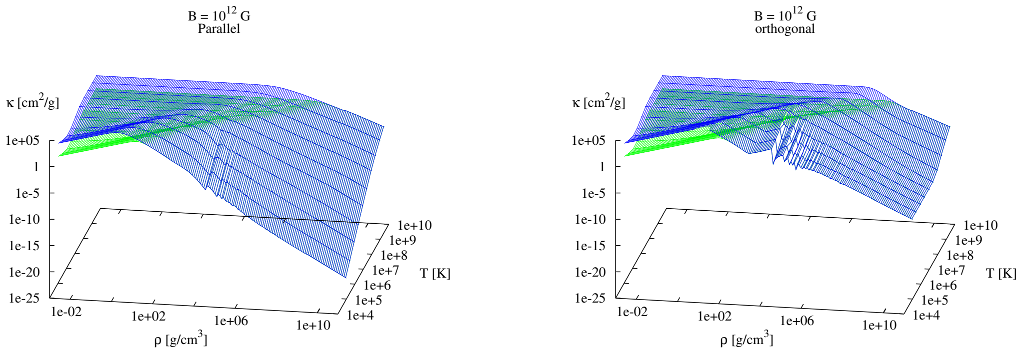

Figure 4.7: The total opacity surfaces in the case where $B = 10^{12}$ G. In the left panel we plot the parallel case and the right panel is the orthogonal case. In both graphs, the lower surface shows the case where $\alpha = 1$ and the upper one is the case where $\alpha = 300$. Notice that the ridge where the opacity changes from $\kappa_{\rm rad}$ dominated to $\kappa_{\rm con}$ dominated shifts to lower densities as α is raised.

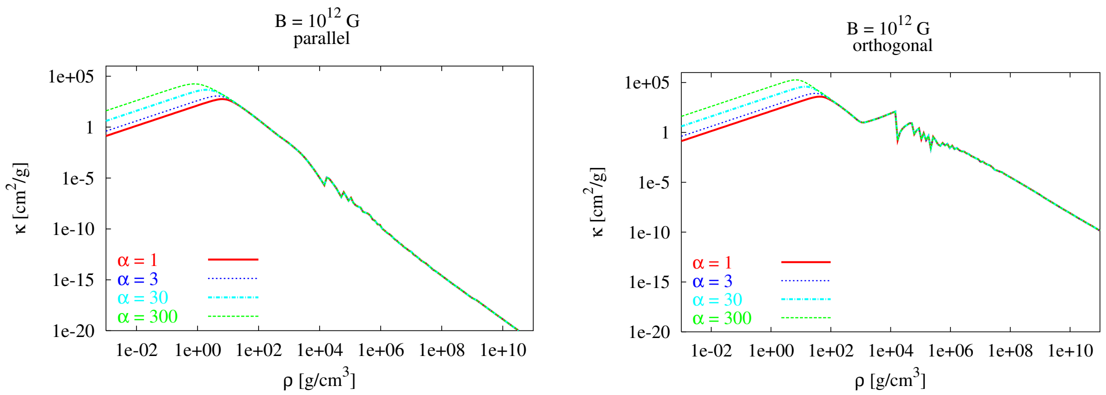

Figure 4.8: The $B = 10^{12}$ G total opacity graphs at low temperature ($T = 10^5$ K) for various values of α. The left panel shows the parallel case and the right panel the orthogonal. The graphs are plotted to the same scale for comparison.

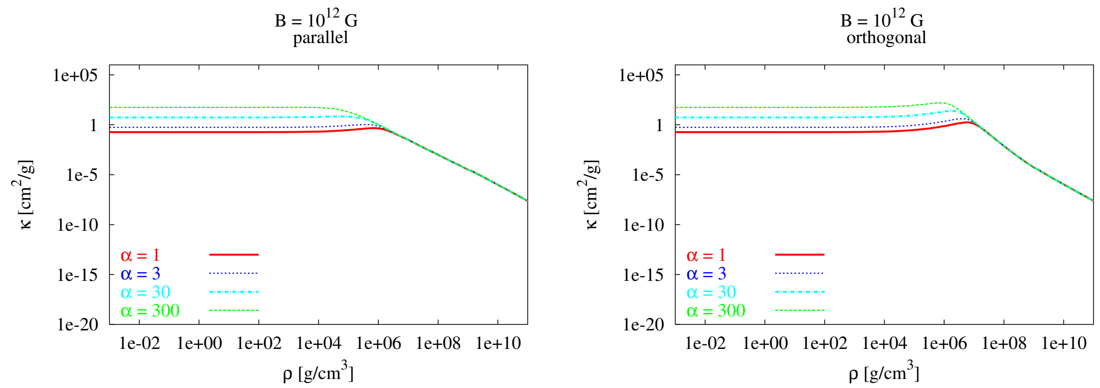

Figure 4.9: The $B = 10^{12}$ G total opacity graphs at high temperature ($T = 3 \times 10^8$ K) for various values of α. The left panel shows the parallel case and the right panel the orthogonal. The graphs are plotted to the same scale for comparison.

where $\kappa_{\rm SY}$ is the radiative opacity, as calculated using the method in [24], and $\kappa_{\rm AP}$ is the electron conduction opacity, as calculated with the use of Potekhin's code.

In figure 4.7, we plot the resulting total opacity as a function of both temperature and density, in the case where $B = 10^{12}$ G. Shown are the two extreme cases where $\alpha = 1$ and $\alpha = 300$. Corresponding surfaces for all intermediate values of α lie between these two surfaces. Further comparisons of $\kappa_{\rm tot}$ with different values of α can be seen in figures 4.8 (at low temperature) and 4.9 (high temperature).

In chapter 6, we investigate the effect of α on our internal temperature results. There we will show that setting $\alpha = 1$ gives the results that best match the results of earlier workers.

We plot the total opacity surfaces for the four values of magnetic field strength, and in the case where $\alpha = 1$, in figures 4.10 (parallel case) and 4.11 (orthogonal). For easier comparison, all the panels are plotted in the same scale and from the same viewing angle. We note how the bulge where $\kappa_{\rm rad} \approx \kappa_{\rm con}$ shifts slightly to higher densities and the grooves in the conductive regime deepen as the field increases. This bulge shows approximately the location of the *sensitivity strip*, an elongated area in the $\rho - T$ plane, first found by Gudmundsson et al. [8], where our method for finding the internal temperature is especially sensitive to errors in the opacity.

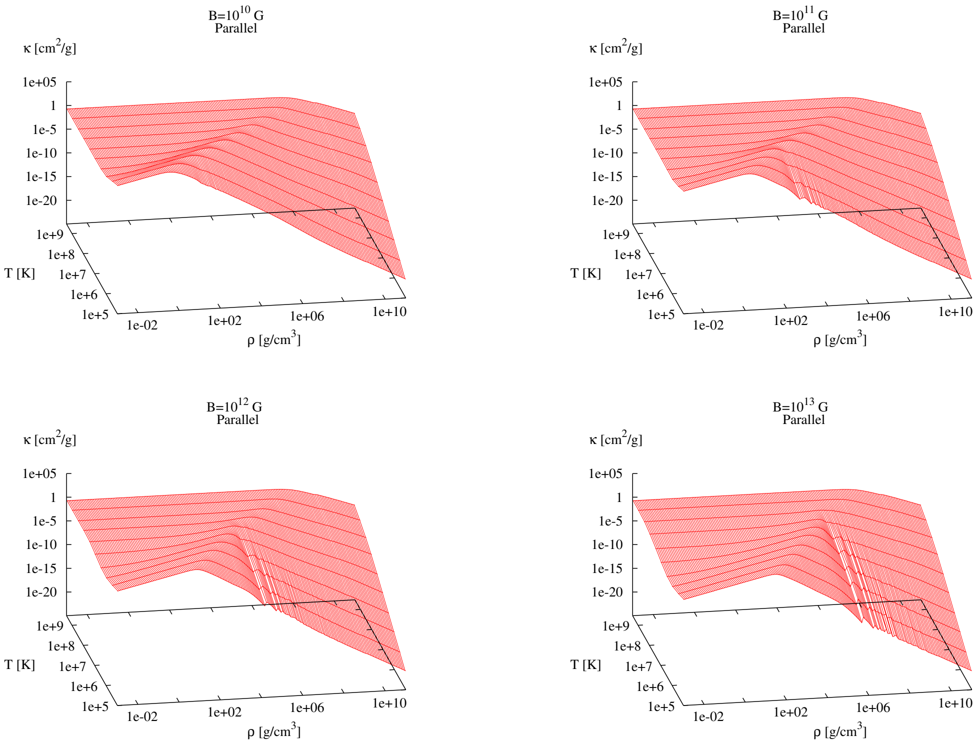

Figure 4.10: Total **parallel** opacity in the case where $\alpha = 1$ as a function of both density and temperature. Each panel represents a different magnetic field strength.

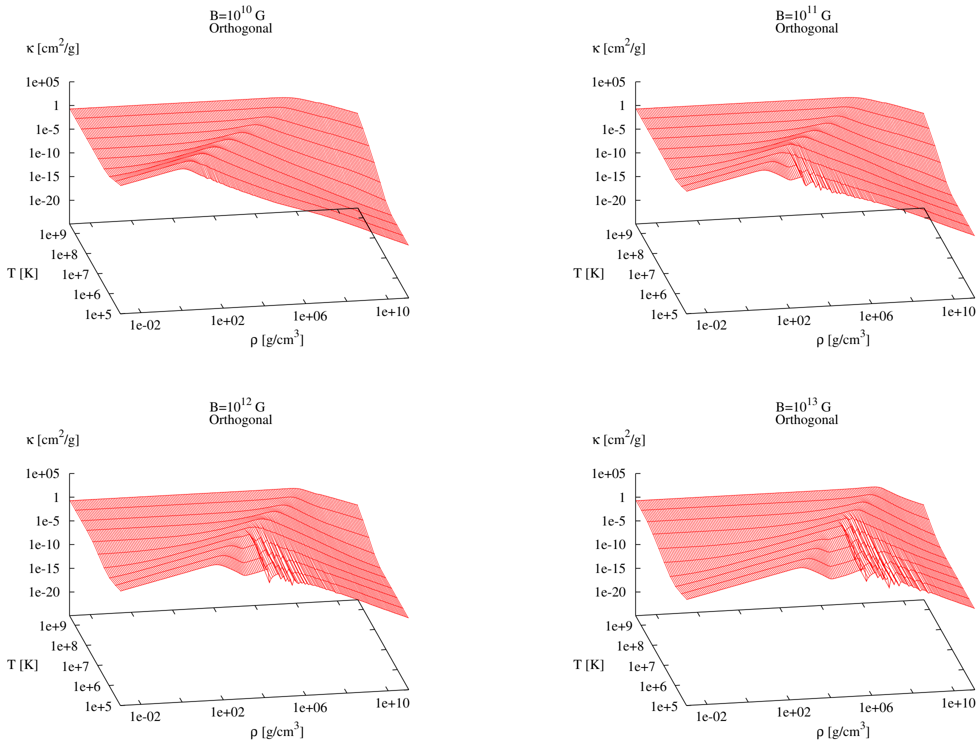

Figure 4.11: Total **orthogonal** opacity in the case where $\alpha = 1$ as a function of both density and temperature. Each panel represent a different magnetic field strength.

Chapter 5

Numerical Calculations

In this chapter we discuss the formulae, methods and programs we use in our code to obtain the surface-core temperature relation.

5.1 Calculations

We have done our programming in Fortran 90. All calculations are executed in double precision and care is taken to give all numerical and physical constants with accurate values, to as many digits as possible. This is done to guarantee that the code itself is not a source of error, so that it can be reused later with future physical input. For the numerical integration, we use a fifth order Runge-Kutta method with adaptive step size. The algorithm is further described in Press et al. [21, chapter 16.2].

For our equation of state, we have constructed a table of the electron pressure values for a grid of ρ and T values. We have also constructed similar tables for the opacity. The pressure and opacity is calculated at each step of the integration by interpolating within the appropriate table. The interpolation is linear in the logarithm of the variables ($\log\rho$, $\log T$, $\log P$ or $\log\kappa$). The pressure gradients, $(\partial P/\partial\rho)_T$ and $(\partial P/\partial T)_\rho$ (cf. equation (2.17)) are calculated linearly from the nearest neighbours. We note again that the tabulated pressure is only available as a function of density and temperature for five values of the temperature.

In the absence of magnetic fields, the thermal structure of neutron star envelopes is governed by a single factor, the Eddington number: $\mathcal{E} = T_{\mathrm{s}}^4/g_{\mathrm{s}}$, once the equation of state and the opacity are given [8]. However, when a strong magnetic field is

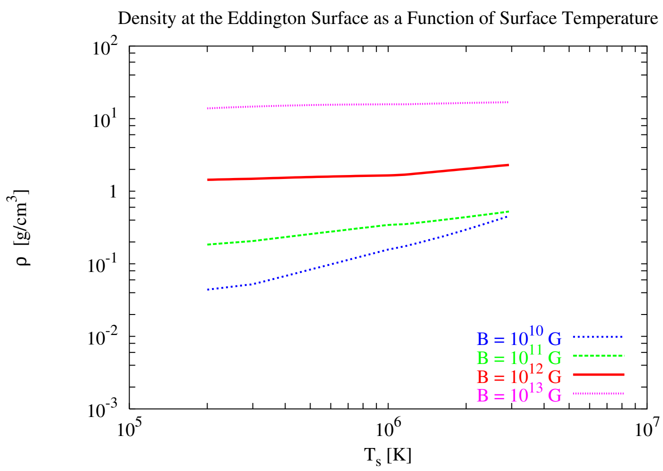

Figure 5.1: Here we plot the solution, $\rho_{\rm s}$ to Eddington's criteria (5.1) as a function of $T_{\rm s}$ for all the four values of magnetic field strength. For all the curves we have set $g_{\rm s} = 10^{14}$ cm/s^2, $\alpha = 1$ and $\psi = 0°$. We can see how increasing the magnetic field pushes the stellar surface (defined at optical depth of 2/3) to a higher density. The knee we see around $T_{\rm s} = 1.2 \times 10^6$ K is an artifact that stems from too coarse an equation of state.

present, its field strength and direction need to be taken into account. In addition, the inaccuracy in our radiative opacities introduces another variable, α, as discussed in chapter 4. Thus, before we start calculating a model we need to specify five constants: $\mathcal{E}$ (or $g_{\rm s}$), $T_{\rm s}$, B, ψ, and α.

When these constants have been specified, the next step is to solve Eddington's surface criteria for a grey atmosphere:

$$P_s(B, \rho_{\rm s}, T_{\rm s}) = \frac{2}{3}\frac{g_{\rm s}}{\kappa(B, \psi, \alpha, \rho_{\rm s}, T_{\rm s})}. \tag{5.1}$$

For the initial conditions, we solve equation (5.1) numerically using Brent's method [21, chapter 9.3]. In figure 5.1 we plot a few sample solutions to equation (5.1), $\rho_s(T_{\rm s})$, for the case where $g_{\rm s} = 10^{14}$ cm/s^2, $\psi = 0°$ and $\alpha = 1$. We are interested in $T_{\rm s}$ in the range 3×10^5 – 3×10^6 K. After the initial conditions have been set, the integration steps can be taken. After each step of the integration, the numerical error is evaluated and the result is fed back, affecting the step size. A proportional error much smaller than a given tolerance level (in our case 10^{-5}) leads to a larger next step but an error larger than the tolerance level leads to the last step getting discarded, the step size reduced and the step taken again. The calculations are stopped if one of the following criteria is fulfilled:

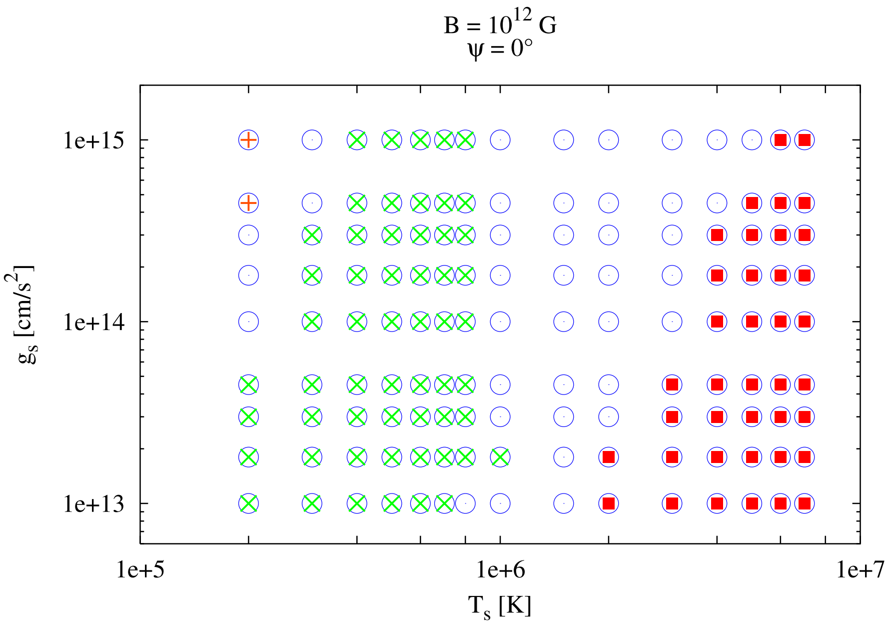

Figure 5.2: The (T_s, g_s) parameter space. Shown is the case where $B = 10^{12}$ G, $\psi = 0°$ and $\alpha = 1$. The circles represent points in the $(T_s,\ g_s)$ space where we have calculated an envelope model. Inside the circles are symbols which label the result of the calculations. The circles in the upper-left corner with a + symbol signify points where we can not find the starting ρ_s by use of Eddington's criteria (5.1). In these cases, ρ_s is arbitrarily set at 0.1 g/cm^3. The $\times$-symbols mark envelopes in which the density gradient became momentarily negative. The ■ mark the envelopes where the internal temperature is higher than the maximum temperature for our equation of state and opacity tables. The $\odot$ mark the envelopes that were integrated without problems (see text for details).

1. The density exceeds $\rho_{\max} = 1.3 \times 10^{11}$ g/cm^3. At this point we have come sufficiently close to the neutron drip point that all thermal profiles have become flat.

2. The temperature exceeds $T_{\max} = 1.1 \times 10^9$ K. This stems from the limitation of the equation of state tables.

3. The number of steps exceeds $N_{\max} = 4000$. We found that our algorithm needs at most 500—1000 steps to finish a single profile.

5.2 The (T_s, g_s) Parameter Space

We have tried our program on several (T_s, g_s) values. In figures 5.2 (parallel) and 5.3 (orthogonal) we show the outcome of those calculations in the case where $B =$

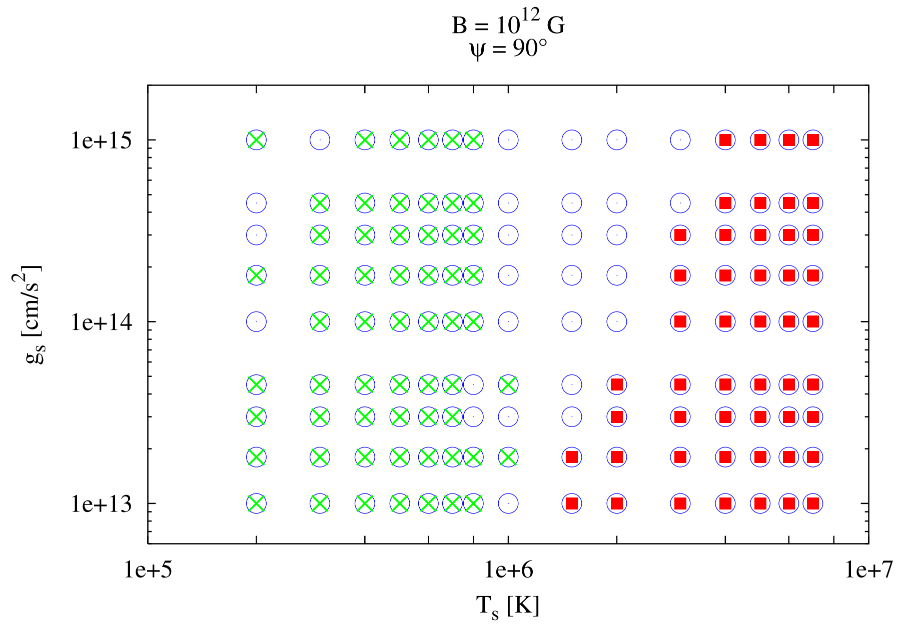

Figure 5.3: The same as in figure 5.2 but for $\psi = 90°$.

10^{12} G, $\psi = 0°$ and $\alpha = 1$. We draw a circle corresponding to each envelope model calculated and inside each circle we draw a symbol representing the outcome of the calculations.

A $\cdot$ inside the circle means that no problem was encountered.

A $+$ indicates that equation (5.1) has no solutions, ρ_s, within our parameter range. In these cases we have set ρ_s arbitrarily at 0.1 g/cm^3. As we will show in chapter 6, this does not affect our resulting internal temperature.

A $\times$ indicates that at some point in the integration at least one step was taken where the density gradient became negative: $d\rho/dz < 0$. We will discuss the effect of this in chapter 6.

And finally, a $\blacksquare$ indicates that the calculations are stopped because the temperature has exceeded the maximum temperature for which we have a reliable equation of state, $T_{\max} \approx 1.16 \times 10^9$ K.

Chapter 6

Results

In this chapter we present our results for the thermal structure of neutron star envelopes. We investigate the dependence of the thermal structure on the α-parameter, the magnetic field strength and direction as well as the Eddington number. We investigate the surface-internal temperature relationship and compare our result with that of previous authors.

6.1 Sample Thermal Structures

As discussed earlier, we have integrated equations (2.17) and (2.16) to build a thermal model of neutron star envelopes. In figure 6.1 sample thermal profiles for $B = 10^{10}$, 10^{11}, 10^{12} and 10^{13} G are shown. From the figure we see that with increasing magnetic field strength, the stellar surface (where Eddington's criteria is met and the curves start) is pushed to higher density. With increasing field strength, the internal temperature for a given surface temperature drops slightly. Thus, the knee (at $T \sim 10^8$ K and $\rho \sim 10^5$ g/cm^3) is sharper at higher magnetic fields. In all four curves the thermal gradient becomes small already at density $\rho \sim 10^7$ g/cm^3.

Another feature that we can see from these sample profiles is a small shift that occurs at $T \sim 10^6$. This is not a physical feature, instead it stems from the "roughness" of the pressure tables. In this region the equation of state tables are only available as a coarse function of temperature so the pressure gradient jumps discontinuously around the tabulated values. This leads to the kink in the thermal profiles at $T \sim 10^6$ K. Looking back at equation (2.17) we see that the density gradient

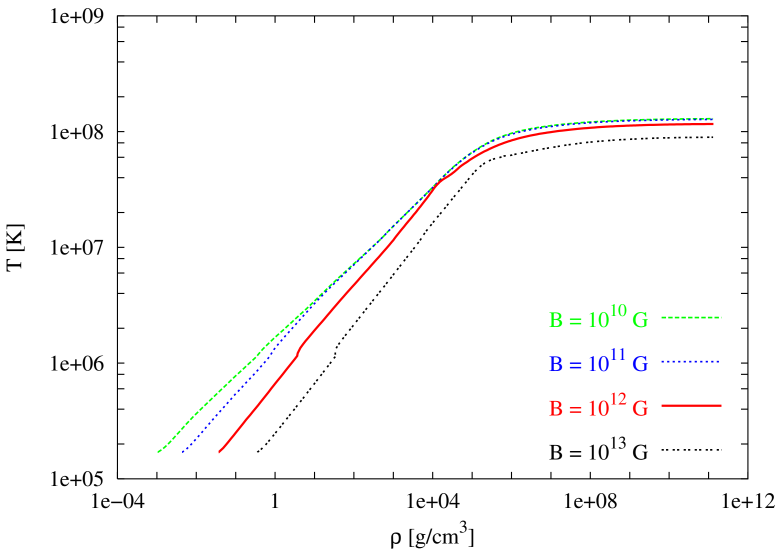

Figure 6.1: Sample thermal profiles, T as a function of ρ. Each curve corresponds to a fixed magnetic field strength, B. For all the curves we have set $\psi = 0$, $\mathcal{E} = 10^{10}$ g $\mathrm{K}^4/\mathrm{dyn}$ and $\alpha = 30$. Refer to the discussion in the text for explanation. Here, the profiles start at $T_\mathrm{s} = 1.7 \times 10^5$ K.

becomes negative only when the condition:

$$1 < \left(\frac{\partial P}{\partial T}\right)_\rho \frac{3}{16}\frac{T_\mathrm{s}^4}{g_\mathrm{s}}\,\frac{\kappa}{T^3} \tag{6.1}$$

is met. Fortunately, this only occurs in the outermost layers of the envelopes (typically where $\rho < 10^2$ g/cm^3), where even sizeable errors in the thermal profiles quickly correct themselves. This we can see from figure 6.2, where we have plotted thermal profiles in the $B = 10^{12}$ G case for various arbitrary initial conditions but keeping the Eddington number fixed (at $\mathcal{E} = 10^{10}$ K^4 g/dyn). All the curves converge quickly, leading to the same thermal structure at higher densities and the same internal temperature, T_b. Even with strongly perturbed initial conditions the curves "find the way" to the right solution, in accordance with the results of Gudmundsson et al. [8]. We can therefore safely assume that this numerical artifact does not alter our resulting internal temperature.

In figure 6.3 we show the profiles from figure 6.2 superimposed on the pressure surface presented in chapter 3. We can confirm from this figure that the curves do not enter the part of the surface where the radiation pressure dominates (the ramp in the upper left corner) unless they are artificially allowed to begin there. Similarly, in figure 6.4 we draw the same profiles superimposed on the opacity surface.

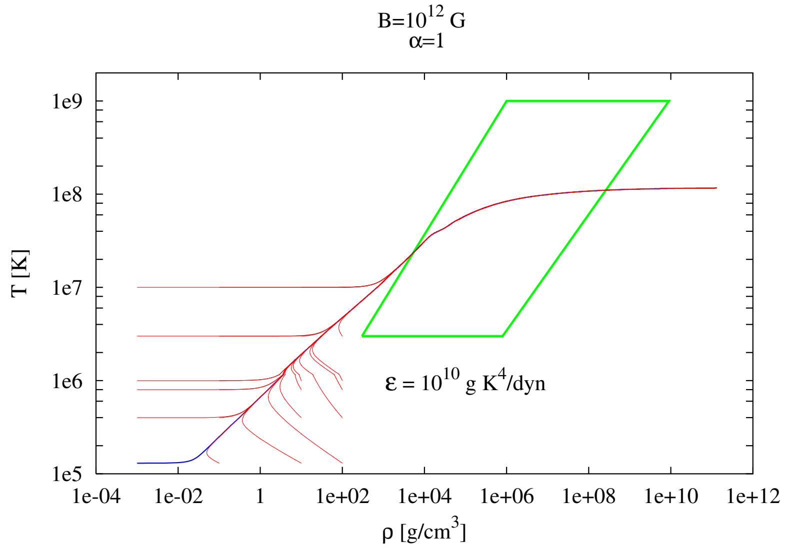

Figure 6.2: In this figure we have plotted thermal profiles for various initial conditions but a fixed Eddington number, $\mathcal{E} = 10^{10}$ g K^4/dyn . For all the curves we have set $B = 10^{12}$ G, $\psi = 0°$ and $\alpha = 1$. Here, the initial conditions were arbitrarily set instead of finding the solution to Eddington's criteria (equation (5.1)). We note that all the curves converge rapidly and lead to the same estimate of the internal temperature T_b. The quadrilateral roughly outlines the area of the sensitivity strip, where accurate knowledge of the opacity is particularly important (as found by Gudmunsson et al. [8, fig. 8]).

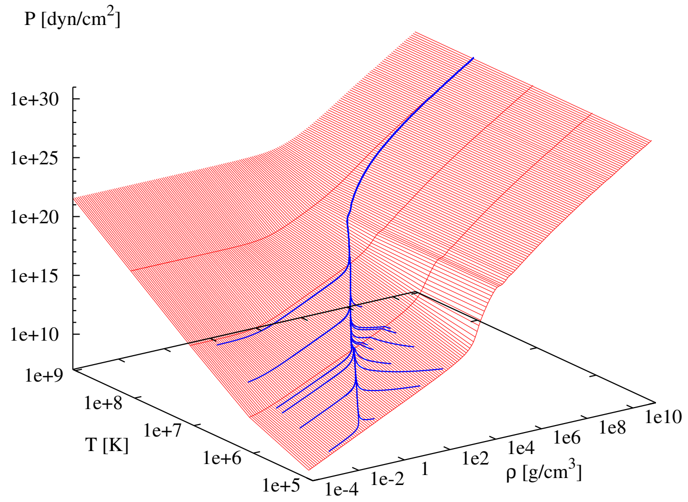

Figure 6.3: The thermal profile curves shown in figure 6.2 and the equation of state surface in (ρ, T, P)-space. Shown is the case where $B = 10^{12}$ G, $\mathcal{E} = 10^{10}$ g K^4/dyn, $\psi = 0°$ and $\alpha = 1$.

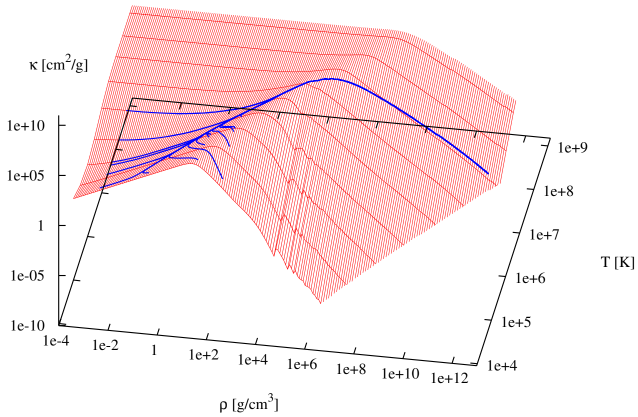

Figure 6.4: The thermal profile curves shown in figure 6.2 superimposed over the opacity surface in (ρ, T, P)-space. Shown is the case where $B = 10^{12}$ G, $\mathcal{E} = 10^{10}$ g K^4/dyn, $\psi = 0°$ and $\alpha = 1$. Notice that we have cut off the corner of the opacity surface at the lowest temperature and highest density. As indicated in figure 6.2, the sensitivity strip is approximately at the knee of the thermal profile.

6.2 Dependence on the α-Parameter

We saw in section 4.2 how the radiative opacity has only been calculated to a factor α. To study the dependence of the thermal structure on the α parameter we have plotted several thermal profiles for various values of α, keeping other parameters constant. The result, for the case where $\mathcal{E} = 10^{10}$ g K^4/dyn and $B = 10^{12}$ G, are shown in figure 6.5. We find that even though α ranges across 2 orders of magnitude, the internal temperatures differ only by $\sim 15\%$ in the parallel case and 60% in the orthogonal case. These results are in agreement with those of Potekhin & Yakovlev [20, Section 2.3.1], who found that as long as the envelope is not too cold the surface-core temperature relation is not noticeably different in the cases of partially ionized and fully ionized envelopes. This can be understood by noting that the radiative opacities are only important at the low density regime of the envelope (see figure 4.7) where, as we have seen, small perturbations tend to correct themselves (figure 6.2).

For the low magnetic field strength of $B = 10^{10}$ G, we expect the magnetic effects to be small, especially at high temperatures. This is supported by our result that the resulting internal temperature is insensitive to ψ in the case of a low magnetic

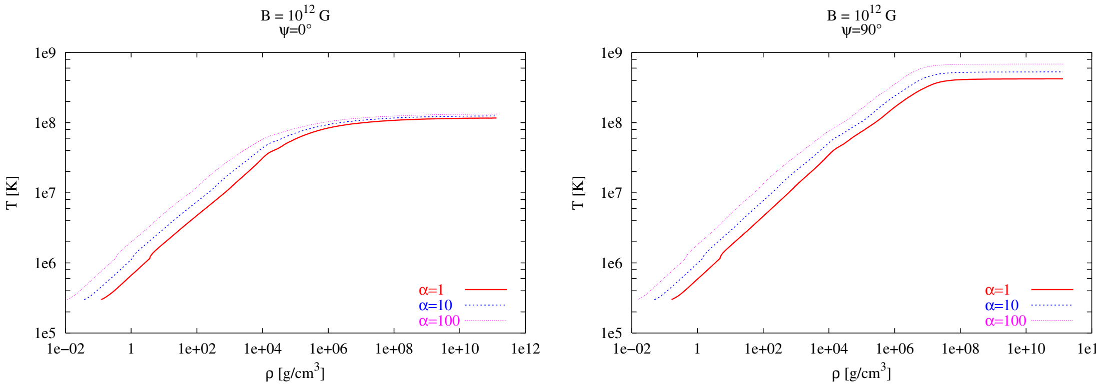

Figure 6.5: Dependence of the thermal profiles on α. The left panel shows the parallel case and the right panel the orthogonal case. In all the curves, we have set $\mathcal{E} = 10^{10}$ K^4 g/dyn and $B = 10^{12}$ G.

field. In figure 6.6 we have compared the relationship between surface and internal temperature from our calculations in the case where $B = 10^{10}$ G to the zero field result of [8]. Shown are, for both the parallel and orthogonal cases, several $\mathcal{E}(T_{\rm b})$ curves, each corresponding to a different value of α. We can immediately see from that figure that indeed $\psi = 0°$ and $\psi = 90°$ lie close to each other (in particular at the higher temperatures). We also see that the best agreement between our results and the zero field result is obtained at $\alpha = 1$. Note that at low temperature, the magnetic effects force the two cases ($\psi = 0°$ and $\psi = 90°$) apart.

As we noted in chapter 4 above, it is reasonable to expect α to be the most important at low density and temperature, in the region where partial ionization might occur. Our method is only sensitive to the value of α at or near the sensitivity strip. In this region, the plasma is fully ionized and α should be set to equal 1.

For these reasons, we choose $\alpha = 1$ as the reference value in our calculations. In figure 6.4 we show how the opacity, $\kappa_{\rm tot}$ (on the z—axis) varies through the envelope (along the thermal profiles) in the case where $\alpha = 1$, $B = 10^{12}$ G and $\psi = 0°$.

6.3 Dependence on Magnetic Field direction

The reader is reminded of the significance of the angle ψ which the magnetic field makes to the vertical (cf. figure 2.3). We mentioned in chapter 4 how the magnetic opacity introduces anisotropy to the problem of thermal transport in neutron star envelopes. We will now investigate the effects on the thermal profiles as a result of varying the angle ψ.

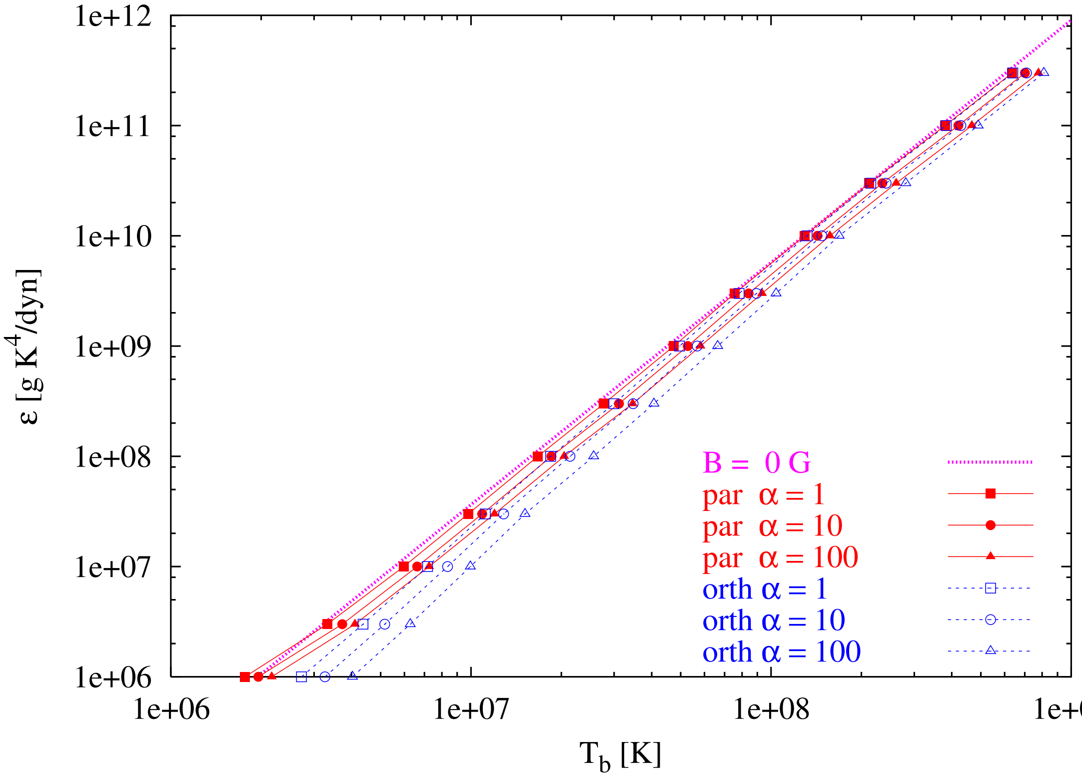

Figure 6.6: In this figure we have plotted the Eddington number, as a function of the internal temperature, T_{b} for various values of α in the case where $B = 10^{10}$ G. Also drawn is the $B = 0$ result from [8]. We see here that $\alpha = 1$ most accurately matches the zero field result, especially at high temperature.

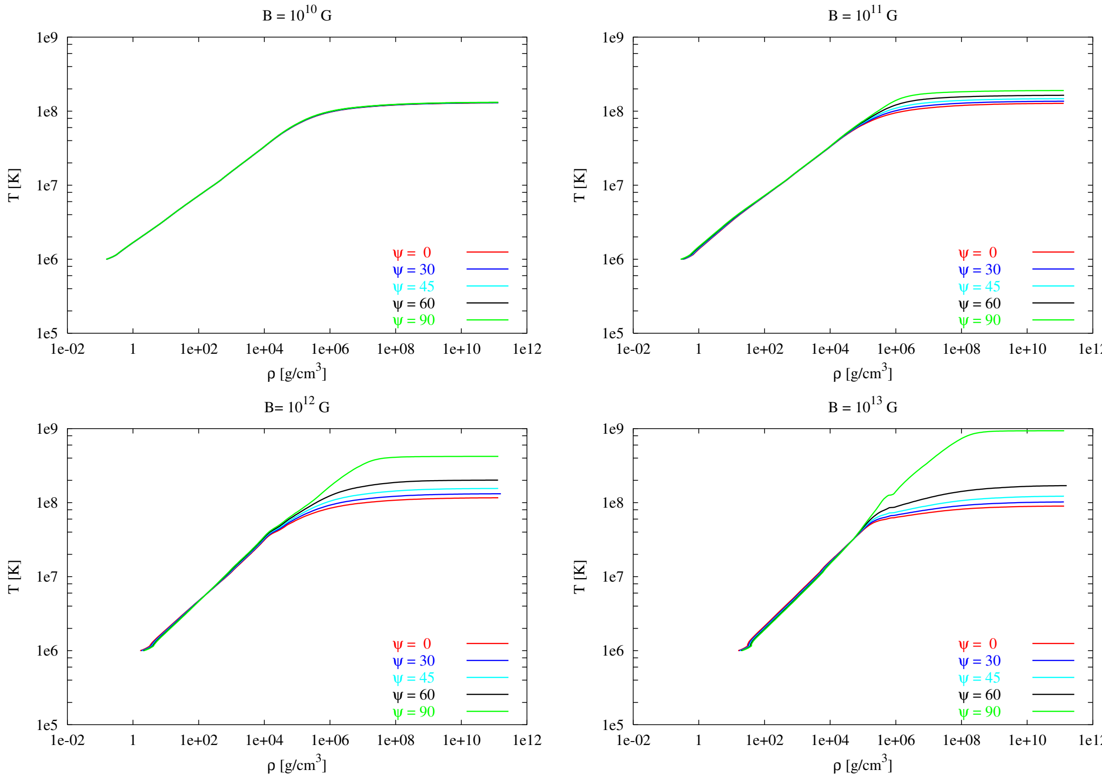

Figure 6.7: Thermal profiles for various angles, ψ, in the case where $\mathcal{E} = 10^{10}$ g $\mathrm{K}^4/\mathrm{dyn}$, $\alpha = 1$ and $T_\mathrm{S} = 1 \times 10^6$ K. Each curve represents the thermal profile for a different value of ψ and each panel corresponds to a different magnetic field strength. For the weakest field, all the curves coincide. In the case of the strongest field, the difference between longitudinal and transverse thermal transport is greater, thus the greater difference in internal temperature (the lowest angles yield the lowest internal temperatures). This is clearly seen in the difference between the upper left panel ($B = 10^{10}$ G) and the lower right ($B = 10^{13}$ G). For clarity, all panels are drawn to the same scale.

In figure 6.7 we present four graphs, one for each magnetic field strength, $B = 10^{10}, 10^{11}, 10^{12}, 10^{13}$ G. In each panel we show five curves, corresponding to the thermal profiles in the case where $\psi = 0°, 30°, 45°, 60°$ and $90°$. From these graphs we can clearly see how the increased magnetic field affects the results leading to widely varying internal temperatures, as expected. Also, we see from these figures that a much greater difference between the temperature at the surface and the core results when the field is horizontal than when it is vertical. Thus, for a given surface temperature, a much greater internal temperature results when the field lies along the horizontal.

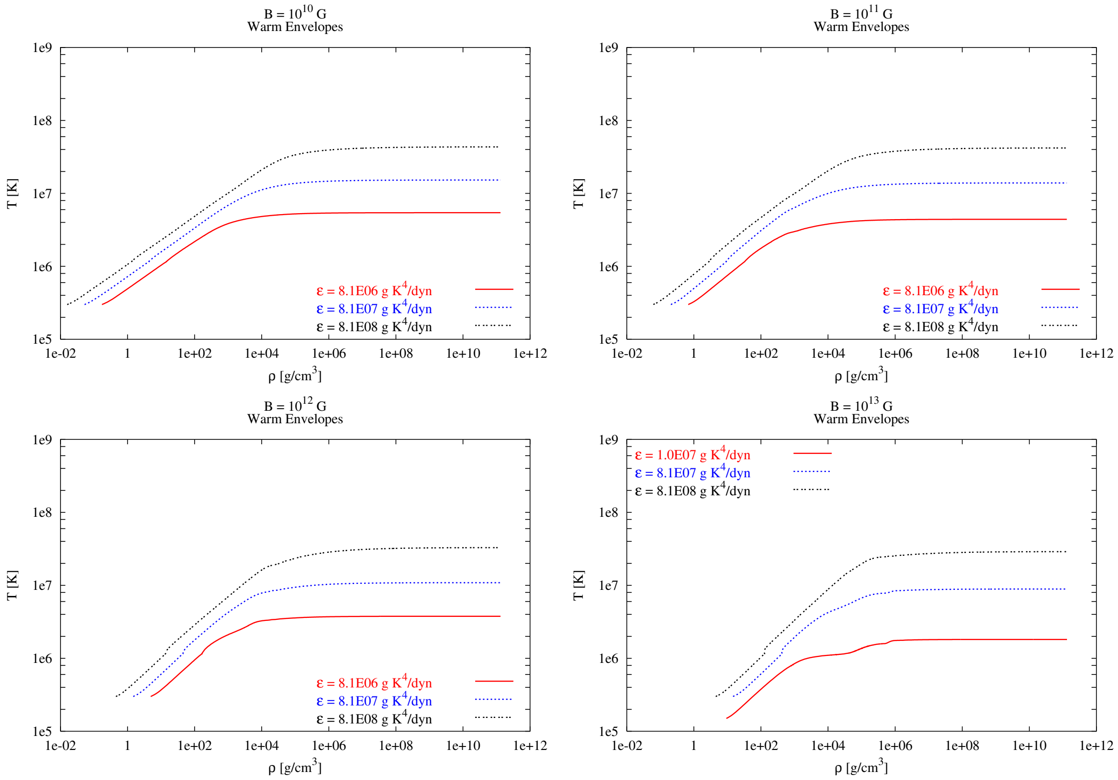

Figure 6.8: Thermal profiles of warm ($T_s = 3 \times 10^5$ K) envelopes for a range of $\mathcal{E}$. Each panel shows the resulting thermal structure for the given magnetic field strength indicated on top of the graph. For all the graphs, we have set $\psi = 0°$ and $\alpha = 1$. $\mathcal{E} = 10^{10}$ g K^4/dyn corresponds to $g_s \approx 10^{15}$ cm/s^2 and $\mathcal{E} = 10^9$ g K^4/dyn corresponds to $g_s \approx 10^{13}$ cm/s^2. See also figure 6.11 and the discussion in the text.

6.4 Dependence on the Eddington number

For isolated neutron stars, the observationally relevant range of T_s is 10^5 – 10^7 K and the surface gravity, g_s, is expected to lie within the range of 10^{13} – 10^{15} cm/s^2 [8]. This corresponds to a range in the Eddington number, $\mathcal{E}$, from 10^5 to 10^{15} g K^4/dyn.

To study the effects of this wide range of plausible $\mathcal{E}$ values, we pick as representative three groups of envelopes which we call *warm* ($T_s = 3 \times 10^5$ K), *hot* ($T_s = 10^6$ K) and *very hot* ($T_s = 3 \times 10^6$ K). Colder neutron stars would lie outside the phase space of our physical input and hotter stars are probably too young for our model since their structure is expected to be dynamic in nature. Each group has its own range of plausible $\mathcal{E}$ values of as shown in the table below:

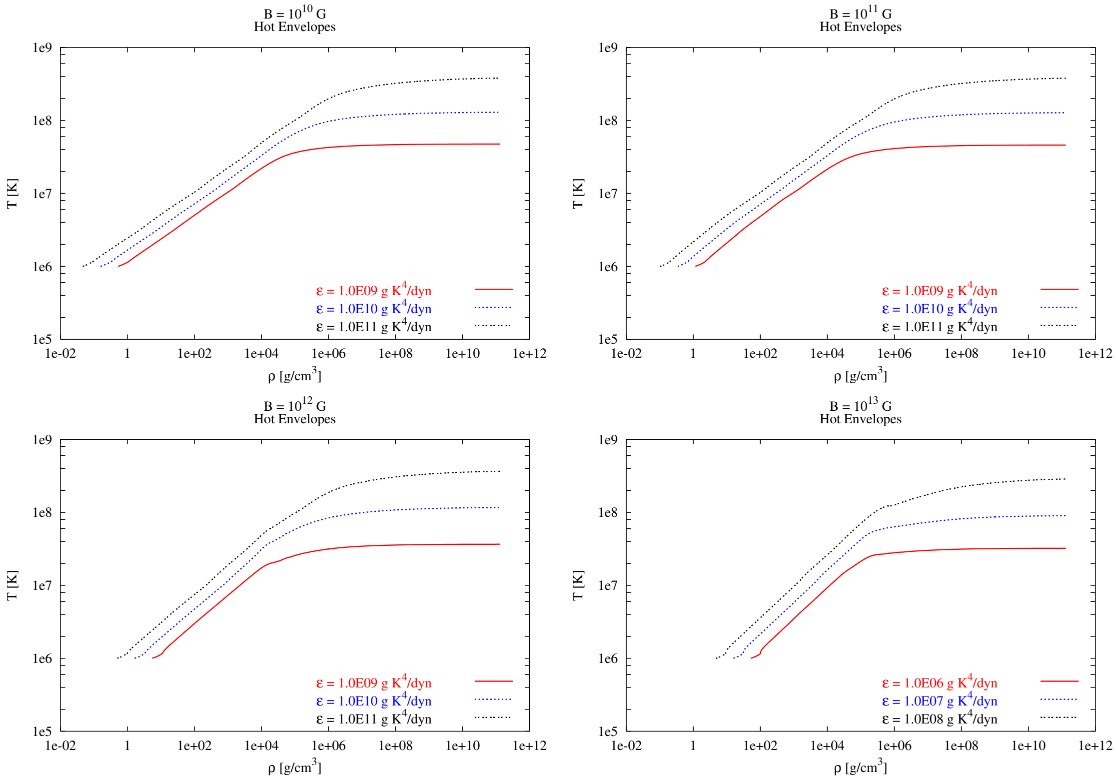

Figure 6.9: Same as the graphs in figure 6.8 but for hot envelopes ($T_s = 10^6$ K). Shown is the parallel case. The scale is the same as in figure 6.8.

Envelope group	T_s [K]	g_s [cm/s^2]	$\mathcal{E}$ [g K^4 dyn^{-1}]
Warm	3×10^5	$10^{13} - 10^{15}$	$\sim 10^7 - 10^8$
Hot	1×10^6	$10^{13} - 10^{15}$	$\sim 10^9 - 10^{11}$
Very Hot	3×10^6	$10^{13} - 10^{15}$	$\sim 10^{11} - 10^{13}$

We use very similar ranges for $\mathcal{E}$ as are used in [8]. For further discussion about the relevant range of initial values we direct the reader there and to Gudmundsson [9].

In each panel of figure 6.8 we plot three thermal profiles corresponding to each order of magnitude in the $\mathcal{E}$ range for warm envelopes. Each panel shows the case of a different magnetic field strength. Similar set of graphs for hot and very hot envelopes can be found in figures 6.9 and 6.10 respectively. We see from these figures that for a fixed T_s, a higher value of $\mathcal{E}$ (i.e. a lower value of g_s) predicts, as expected, a higher internal temperature.

Note that in the case of the warm envelope and $B = 10^{13}$ G, the curve corresponding to the lowest Eddington number starts at $T_s = 2 \times 10^5$ K, whereas the others

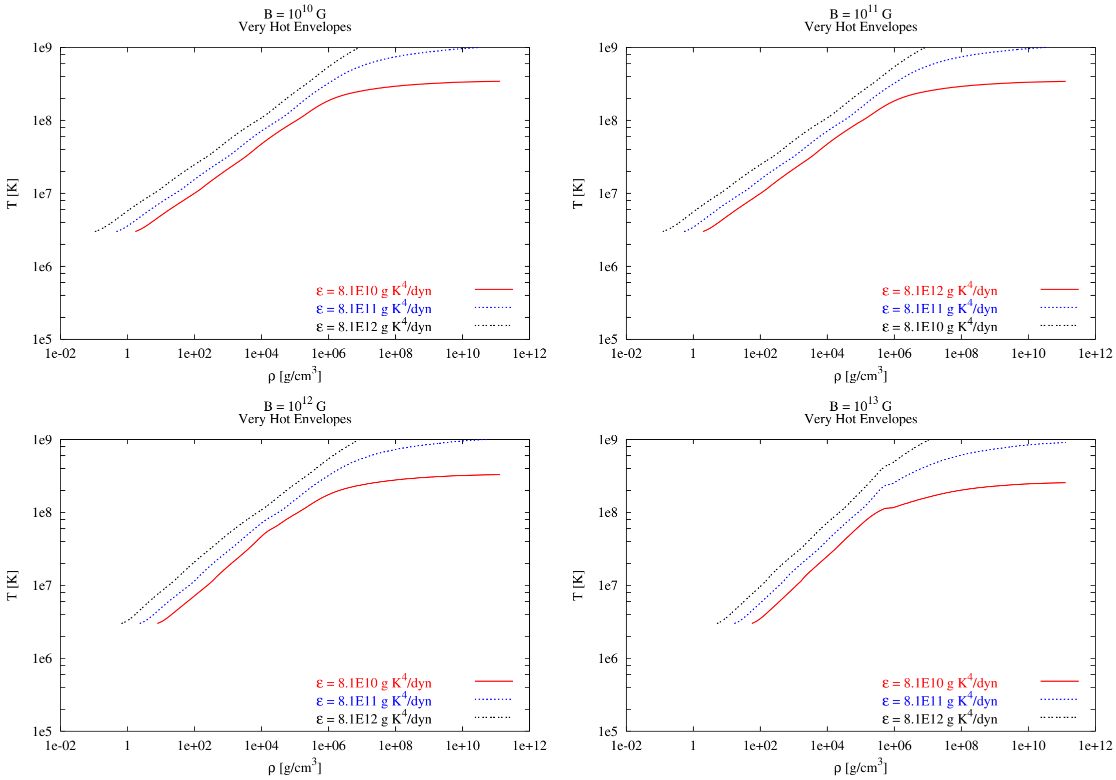

Figure 6.10: Same as the graphs in figure 6.8 but for very hot envelopes ($T_s = 3 \times 10^6$ K). Shown is the parallel case. The scale is the same as in figure 6.8. Here we see that the curves corresponding to $\mathcal{E} \approx 10^{12}$ and 10^{13} g K^4/dyn reach the boundary of our temperature domain and are cut short. As mentioned in chapter 3 our equation of state only covers the temperature range [1.16×10^5–1.16×10^9] K.

start at $T_s = 3 \times 10^5$ K. The reason for this is that for $2.0 \times 10^5 \text{ K} \lesssim T_s \lesssim 5.4 \times 10^5$ K, the solution to Eddington's criteria jumps sharply to a higher density.

We believe this jump to stem from the fact that the physical input is uncertain in this region. At such low temperatures and strong magnetic field, partial ionization makes a possibly important contribution to the radiative opacity. This suggestion is supported by the observation that no such jump occurs if the angle is changed to $\psi = 90°$, as is shown in figure 6.11. In that case, all the temperature curves lie higher. The only angle-dependent part of our physical input is κ. Because of this we shall not include these results in our final analysis of the T_s–T_b relationship (see the next section).

As a neutron star cools, its $\mathcal{E}$ decreases with the fourth power of T (assuming its mass and radius do not change). The entire thermal structure then shifts to a lower temperature, as has be plotted in figure 6.12. Note that this figure gives no

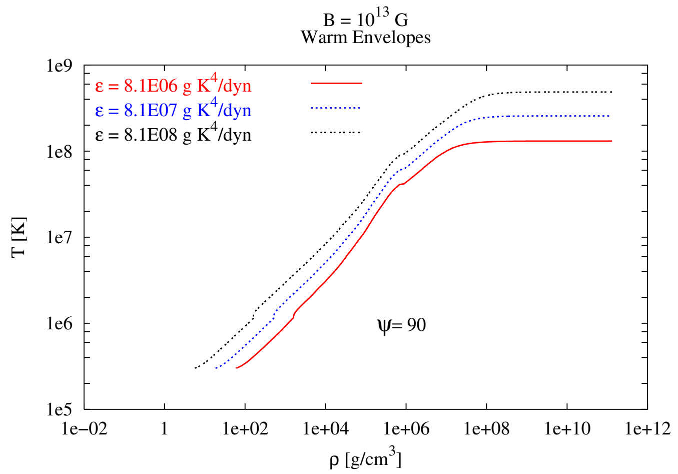

Figure 6.11: Thermal profiles of warm ($T_s = 3 \times 10^5$ K) envelopes for a range of $\mathcal{E}$ in the case where $B = 10^{13}$ G, $\psi = 90°$ and $\alpha = 1$. Compare this figure to the parallel case in the lower right hand panel in figure 6.8. See discussion in text.

information about the cooling rate, only the thermal structure at the moment when T_s is as indicated. In our quasi-static approach, the star's cooling can be visualised by the thermal profile drifting gradually down to lower temperatures.

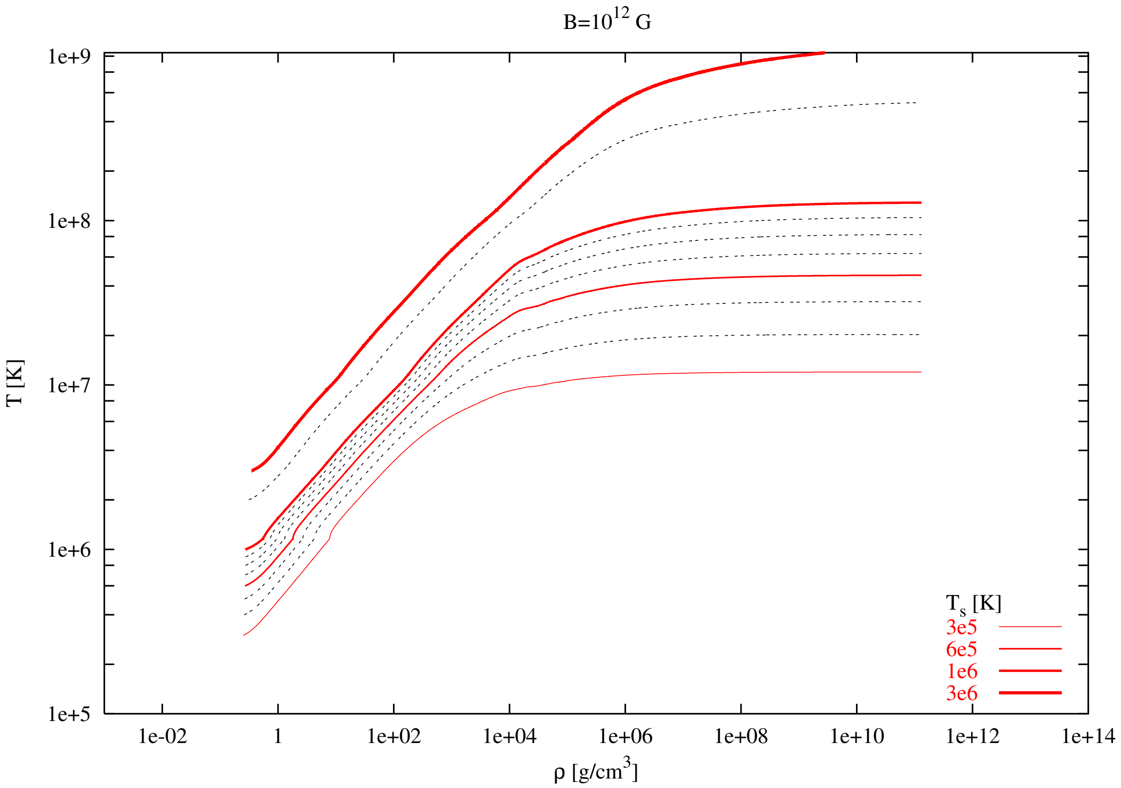

Figure 6.12: Thermal structure profiles in the case where $B = 10^{12}$ G, $\alpha = 30$, $\psi = 0°$ and $g_s = 10^{14}$ cm/s^2. Each curve represents a given surface temperature (and thus a different $\mathcal{E}$). The red solid curves are labelled in the lower right corner. The black dashed curves represent intermittent values of T_s. Note, however that the topmost curve (marked $T_s = 3 \times 10^6$ K) rises above our temperature range ($< 1.2 \times 10^9$ K) before the thermal gradient vanishes.

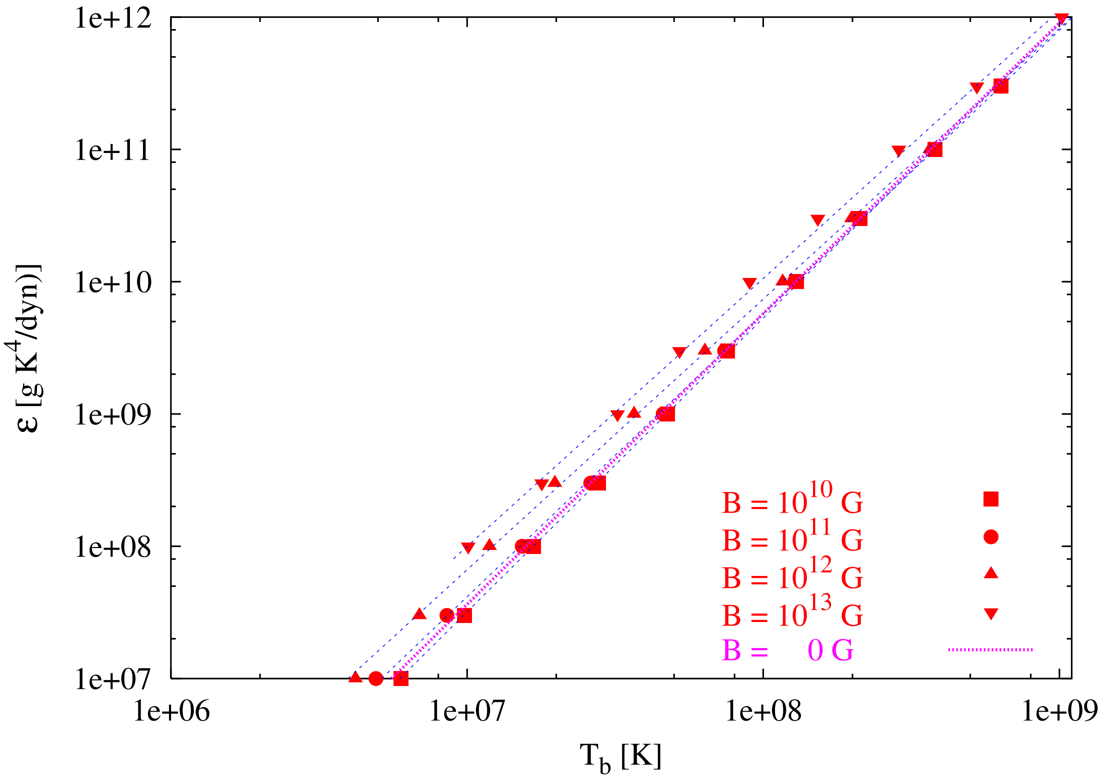

Figure 6.13: The Eddington number as a function of internal temperature for magnetic neutron star envelopes (parallel case). Each point in the graph corresponds to a thermal profile. Shown here is the case where $\psi = 0°$ and $\alpha = 1$. The blue-dashed lines show the fitting formula in each case. The purple dotted line corresponds to the zero field result of [8].

6.5 Core-Surface Temperature Relationship

To investigate the relationship between the surface and internal temperatures we have plotted $\mathcal{E}$ as a function of $T_{\rm b}$. The results are presented in figures 6.13 and 6.14. From figure 6.13 one can see that in the parallel case, when the magnetic field is weak (10^{10} G or 10^{11} G) the magnetic effects are minimal and the curves lie very close to the zero field result almost throughout whole the region of interest. We see a different behavior at $B = 10^{12}$ G (filled triangles, pointing up), where at low temperatures the magnetic field has significant effects. But as the temperature is raised, the effects of B dwindle and the temperature starts to dominate. Hence, the curve merges with the zero field result (at $\sim 2 \times 10^8$ K). Note that in the parallel case, at $B = 10^{13}$ G, we have left out the the two lowest $\mathcal{E}$ points as discussed in the previous section.

As can be seen from both figures, straight lines (on log-log scale) fit the results

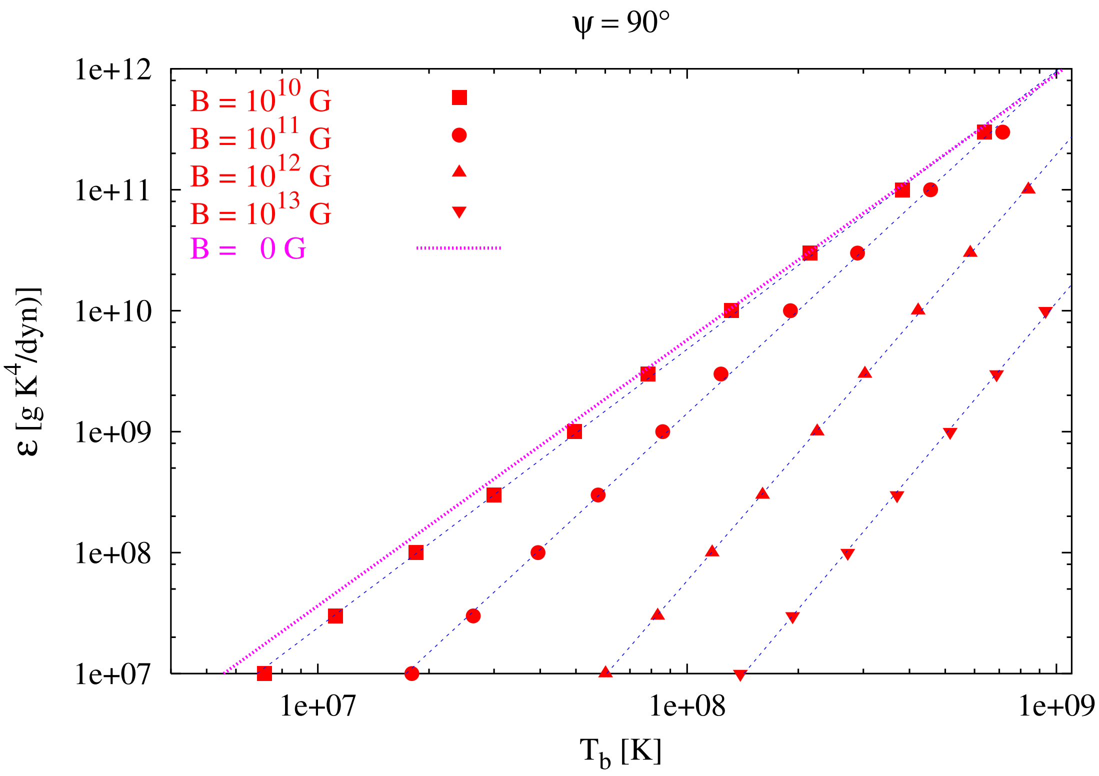

Figure 6.14: Same as in figure 6.13, but for the orthogonal case.

fairly well. Hence a fit of the form:

$$\log(T_{\rm b}) = b\log(\mathcal{E}) + \log(a) \tag{6.2}$$

or, equivalently:

$$T_{\rm b} = a\ \mathcal{E}^{b} \tag{6.3}$$

is in order.

This choice of fitting is done in the spirit of Gudmundsson et al. [8] who found the relationship in the non-magnetic case to be, in cgs units:

$$T_{\rm b} = 3630\ \mathcal{E}^{0.455} \tag{6.4}$$

We use a χ^2 algorithm to achieve the fit. The best fit gave a typical standard error of 1%, but never greater than 2%. In figures 6.13 and 6.14, we have superimposed our fit on our numerical results to demonstrate the goodness of the fit. The resulting

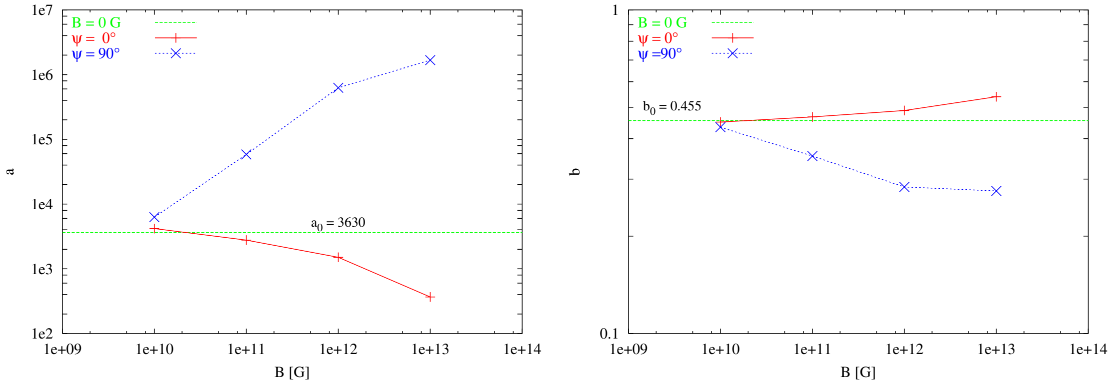

Figure 6.15: The a and b coefficients from the fit shown in figures 6.13 and 6.14 as functions of magnetic field strength. Also drawn are the results of Gudmundsson et al. for the non-magnetic case, $a_0 = 3360$ and $b_0 = 0.455$. As mentioned in the previous section, at weak magnetic fields, both the parallel and the orthogonal coefficients are similar to the zero field results.

coefficients, a and b are given numerically in table 6.1 and are plotted as a function of B in figure 6.15. There, the horizontal lines refer to the zero field result.

B	$\psi = 0°$		$\psi = 90°$	
	$\log_{10} a$	b	$\log_{10} a$	b
0 G	3.560	0.455	3.560	0.4550
10^{10} G	3.622	0.450	3.797	0.434
10^{11} G	3.443	0.467	4.766	0.353
10^{12} G	3.177	0.489	5.797	0.284
10^{13} G	2.565	0.539	6.224	0.276

Table 6.1: The a and b coefficients for the fitting formula, in cgs units. The $B = 0$ G coefficients are taken from [8]. The fits gave a standard deviation of about 1%.

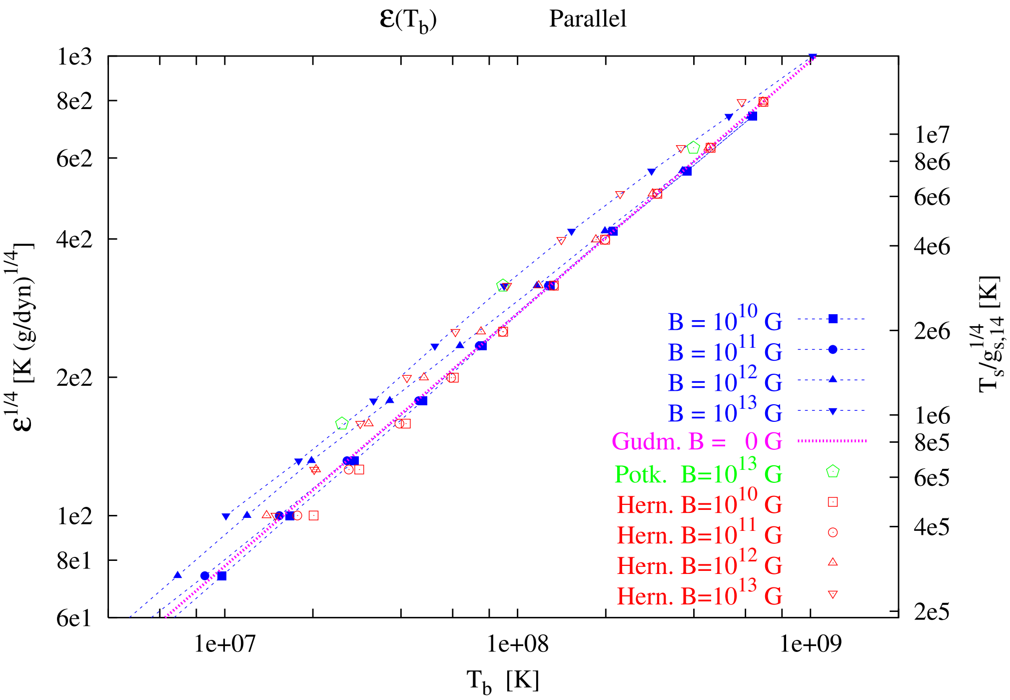

Figure 6.16: A comparison with earlier results in the case where $\psi = 0°$. Shown are the results of our calculations (filled blue marks linked with dashed lines) and the results of [20, Fig. 5] (green pentagons) and [11, Table 1] (red empty symbols). Also drawn is the zero field result of [8] (purple dotted line). For our results, we have set $\alpha = 1$.

6.6 Comparison With Previous Results

We have compared our core–surface temperature relationship with the results of other authors.

We find that our results are in good agreement with the those of Potekhin & Yakovlev [20] as well as those of Hernquist [11]. In figure 6.16 and 6.17 we plot the various results. The scale on the right hand side of these graphs is the scaled surface temperature, $T_{\rm s}/g_{\rm s,14}^{1/4}$, where $g_{\rm s,14} = g_{\rm s}/(10^{14}\ {\rm cm/s})$.

Our results agree very well with the previously published ones. The agreement seems to be best at high temperatures, but the curves diverge slightly at low temperatures. This is especially noticeable in the parallel case where $B = 10^{13}$ G. There, the results of Hernquist [11] predict a much higher internal temperature at the lowest $\mathcal{E}$.

For our calculations, we have used similar opacities as Potekhin & Yakovlev [20] but a different equation of state. Since our results match theirs closely, we conclude that *in the region where* $T_{\rm b} \sim 3 \times 10^7$—$10^9$, and for a given value of B, the $T_{\rm s}$–$T_{\rm b}$

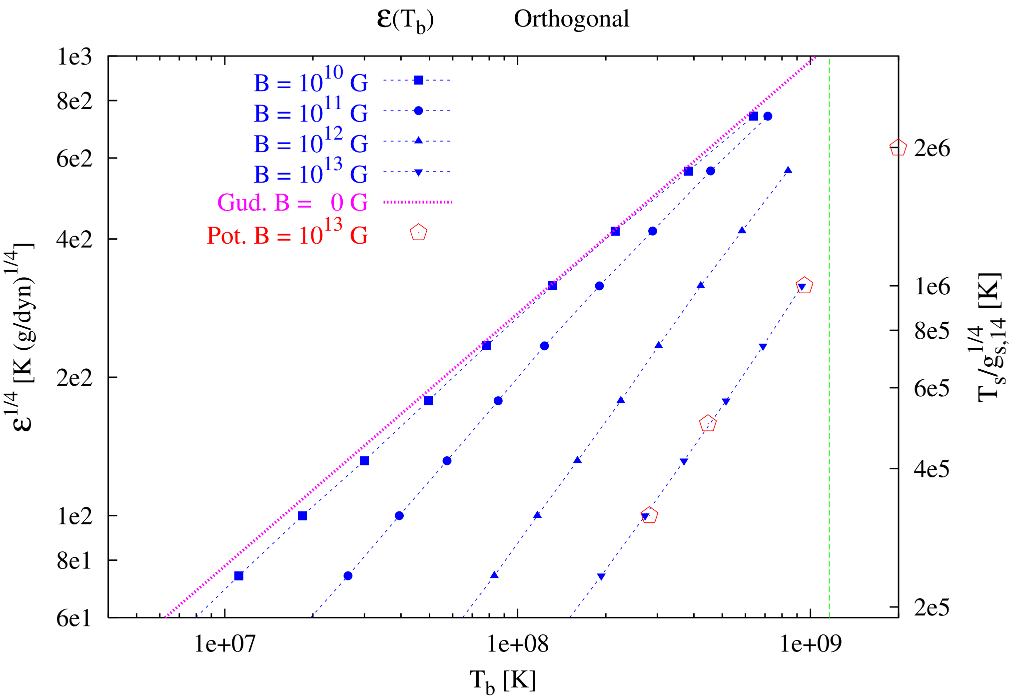

Figure 6.17: Same as figure 6.16 but for the case where $\psi = 90°$. Shown are the results of our calculations (points linked with dashed lines) compared with the results of Potekhin et al. (pentagons). As before, when obtaining our results we have set $\alpha = 1$.

relationship is not very sensitive to the details of the equation of state. We find good agreement even without taking partial ionization into account ($\alpha = 1$). But at the lowest temperatures and strongest fields our results deviate from the trendline as we discussed in the previous section.

Chapter 7

Summary

We have given a detailed description of a known method for studying the quasi-static thermal structure of strongly magnetized neutron star envelopes. We give a description of the state of matter in neutron star envelopes, focusing on the equation of state and the opacity in high magnetic fields. We calculate the thermal structures for a range of neutron star envelopes using the most recent equation of state and electron conductivities. The effects of changing the α and ψ parameters are investigated. By comparing our results with the recent results of Potekhin & Yakovlev [20], we find that, for a given B, the resulting internal temperature is not very sensitive to the details of the equation of state.

We study the relationship between the observable surface temperature of magnetic neutron stars and their core temperature and present fitting formulae of the form:

$$T_{\mathrm{b}} = a\,\mathcal{E}^{b}.$$

We find the coefficients with a standard deviation of $\lesssim 1.5\%$. We have gathered the coefficients in table 6.1. Our results match closely those of previous workers at high temperatures, but diverge somewhat at low temperatures, predicting lower internal temperatures.

Chapter 8

Acknowledgements

I would like to thank my advisor, professor Einar H. Guðmundsson for accurate guidance, warm patience and also for suggesting to me this exciting topic. I had many useful discussions with research professor Gunnlaugur Björnsson, and professor Viðar Guðmundsson has helped me with technical and programming questions, and for that I am grateful. I thank professor Dany Page for his advice and encouragement, as well as Alexander Potekhin for sending us his advice on the opacity and for freely sharing his conductivity code. In addition, I thank my former employer, Garðar Mýrdal for his support and patience.

Last but not least, Viola and Gulli and the rest of my family deserve my sincerest gratitude for their cheerful tolerance and support during this hectic period.

This work was partially funded by a research grant from the Research Fund of the University of Iceland and the Department of Physics of the Science Institute.

Appendix A

The Equation of State Revisited

In the following pages, we will present further graphs of the equation of state. The figures are listed in the table below.

Figure	Short description
Fig. A.1	$P(\rho)$ for fixed T, various B
Fig. A.2	$P(T)$ for fixed B, various ρ
Fig. A.3	Components of $P(\rho)$ at $B = 10^{10}$ G
Fig. A.4	Components of $P(\rho)$ at $B = 10^{11}$ G
Fig. A.5	Components of $P(\rho)$ at $B = 10^{13}$ G

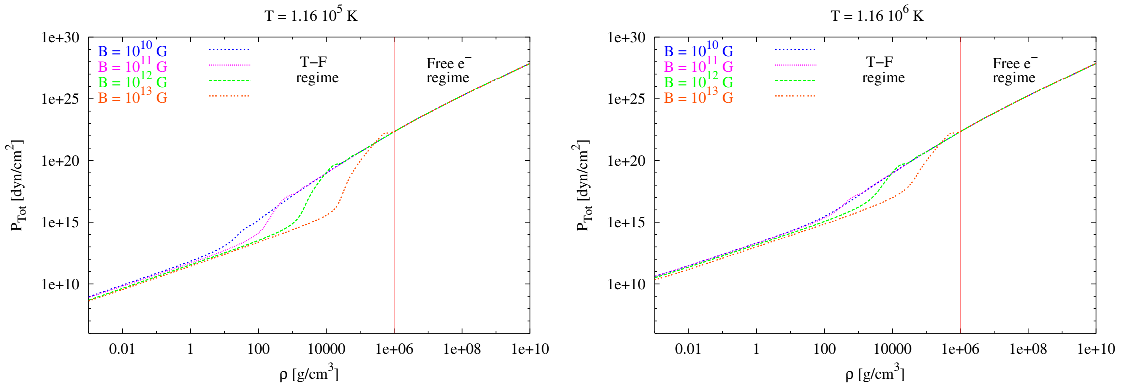

Figure A.1: The total pressure plotted as a function of density. Each curve in the left panel gives the $T = 1.16 \times 10^5$ K isothermal for a given magnetic field strenght. In the right hand panel, corresponding curves for $T = 1.16 \times 10^6$ K are given.

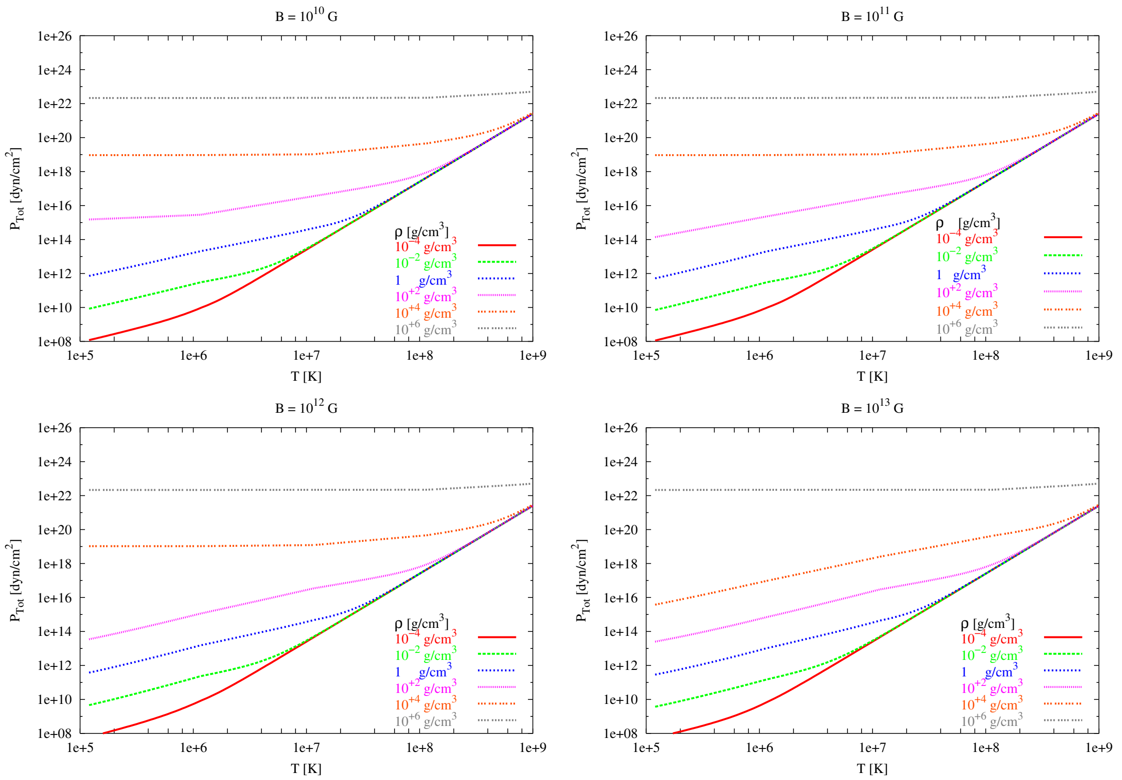

Figure A.2: The total pressure plotted as a function of temperature. Each panel represent a fixed magnetic field. Labelling and scale is fixed between the panels.

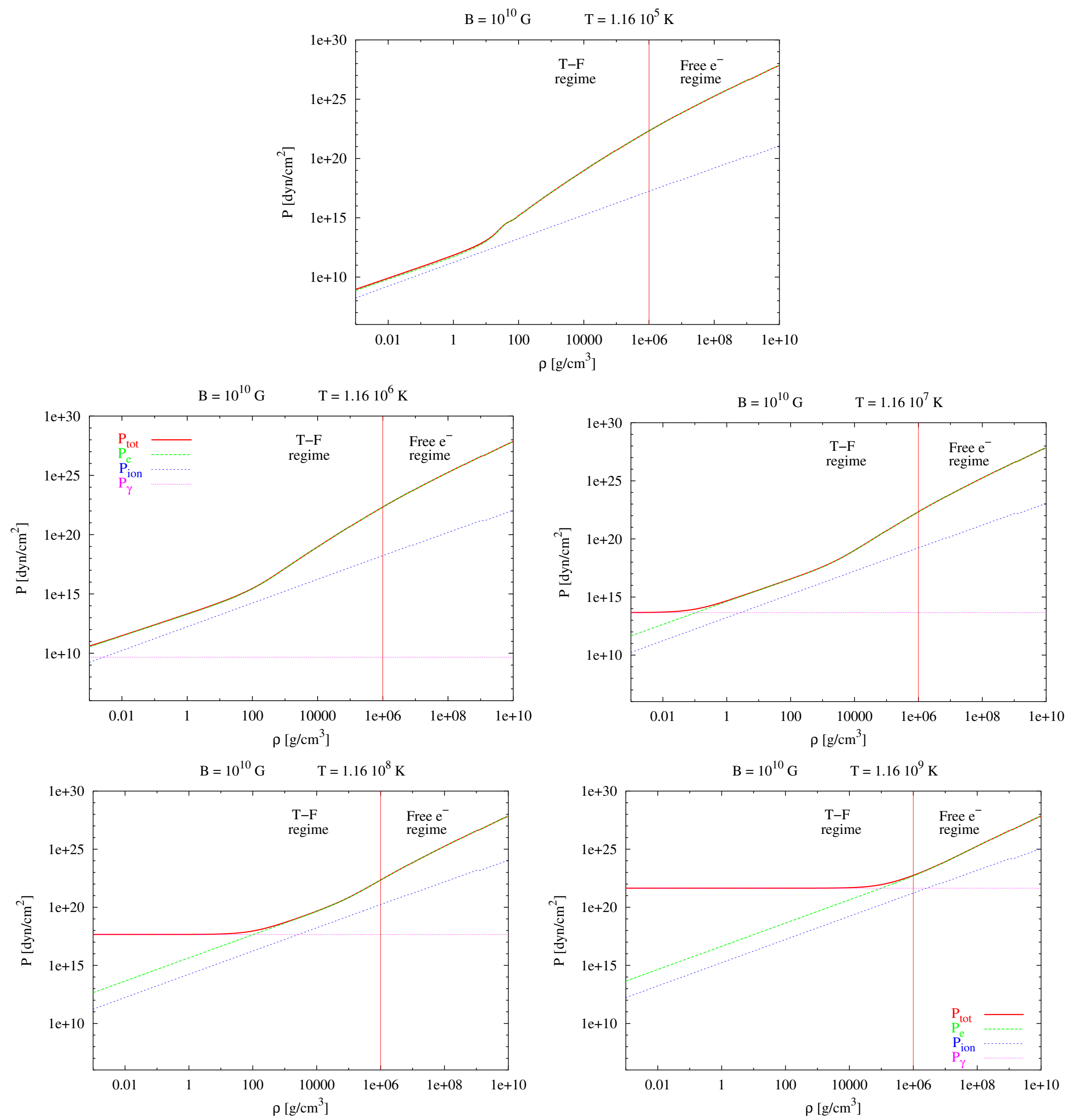

Figure A.3: The pressure terms in the case where $B = 10^{10}$ G. Each panel shows the case for a different value of T (see also figures 3.5 and 3.6). The scale and labelling is held fixed between all the panels.

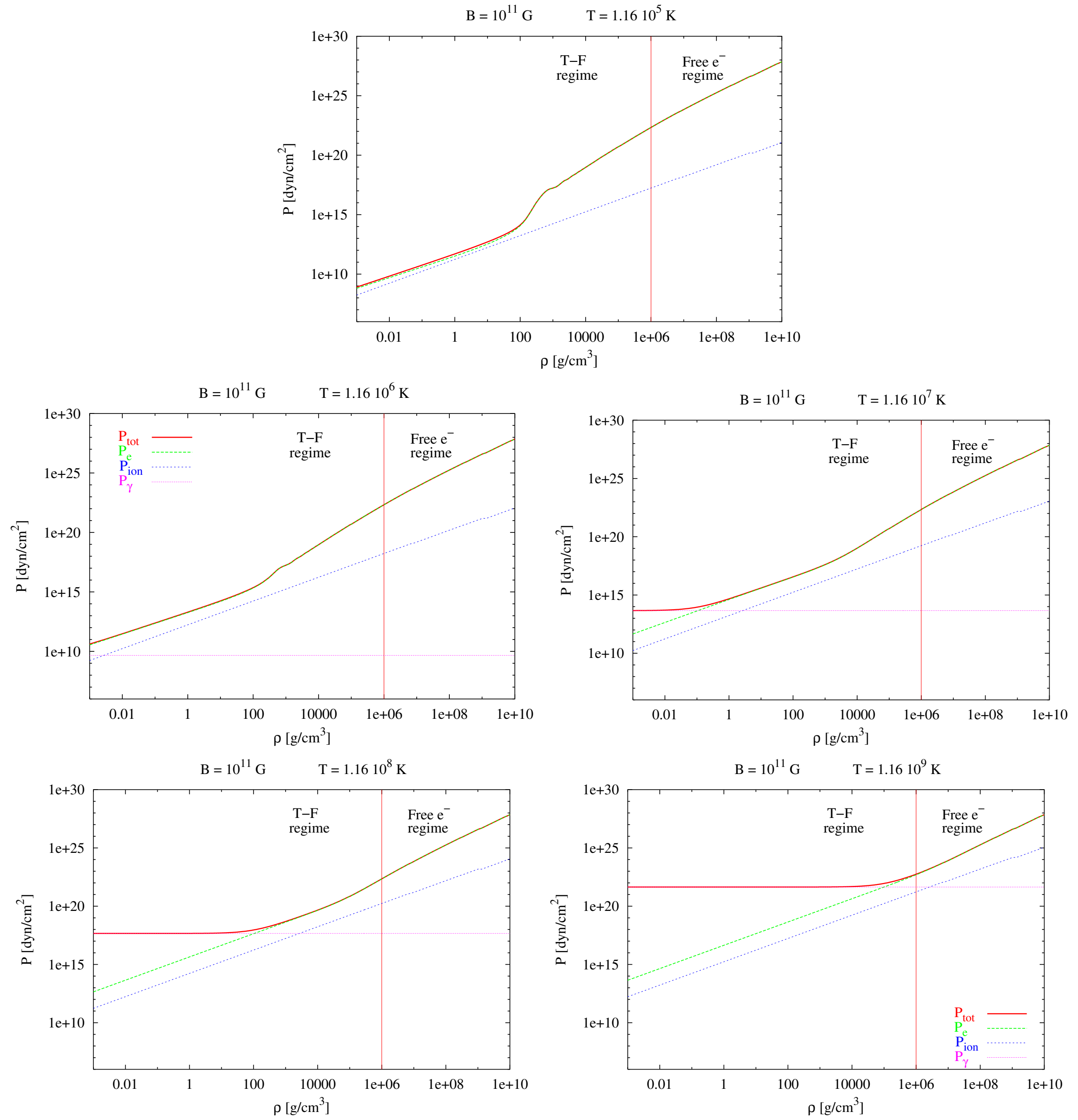

Figure A.4: The pressure terms in the case where $B = 10^{11}$ G (see also figures 3.5 and 3.6). The scale and labelling is held fixed between all the panels.

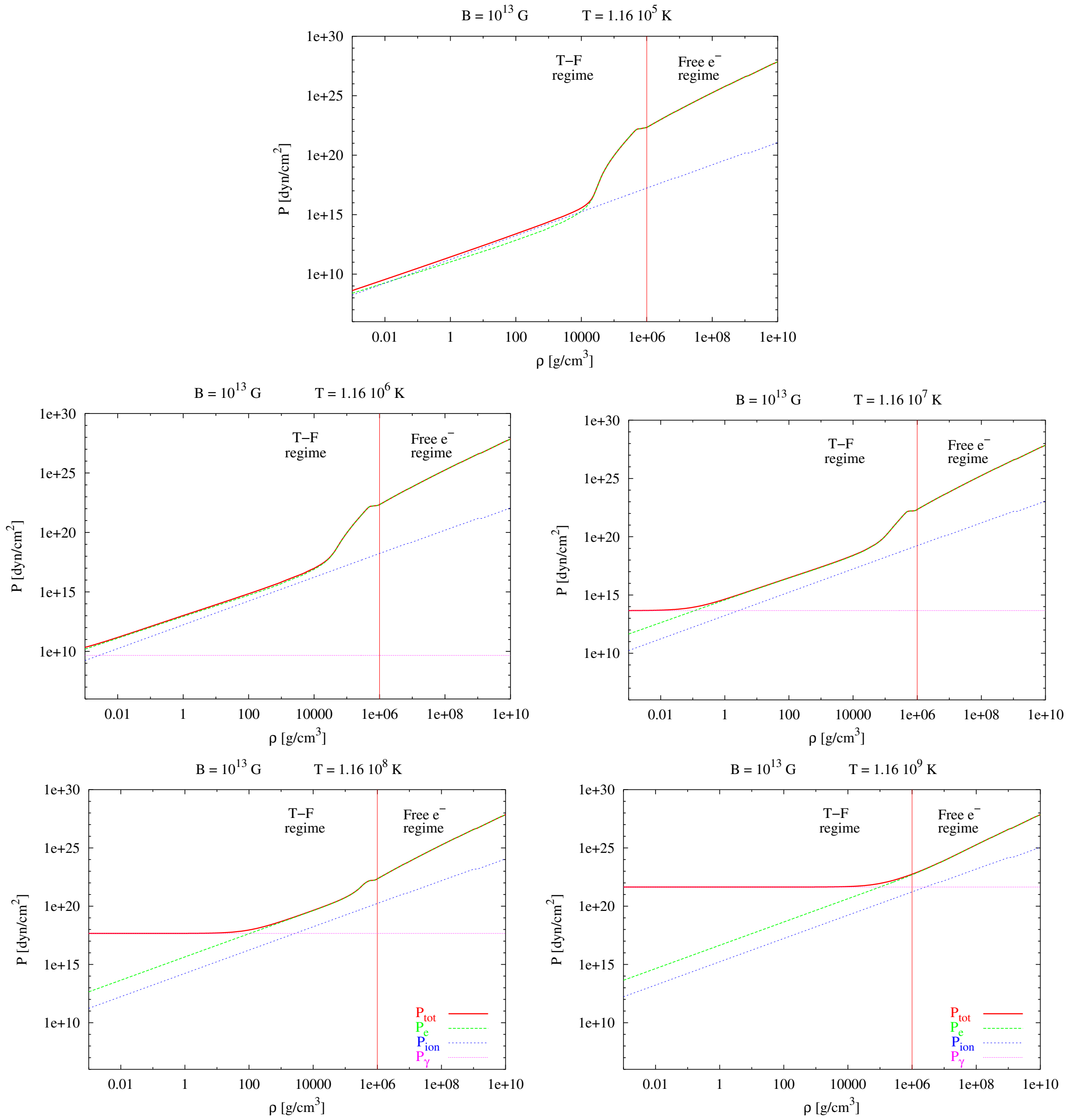

Figure A.5: The pressure terms in the case where $B = 10^{13}$ G (see also figures 3.5 and 3.6). The scale and labelling is held fixed between all the panels.

Appendix B

Further Graphs of the Opacity

In the next few pages we will present a few more graphs of the opacity. The figures are listed in the table below.

Figure	Short description
Fig. B.1	$\kappa_{\|\|}(\rho)$ for low T
Fig. B.2	$\kappa_{\perp}(\rho)$ for low T
Fig. B.3	$\kappa_{\|\|}(\rho)$ for medium T
Fig. B.4	$\kappa_{\perp}(\rho)$ for medium T
Fig. B.5	$\kappa_{\|\|}(\rho)$ for high T
Fig. B.6	$\kappa_{\perp}(\rho)$ for high T
Fig. B.7	The $\kappa_{\|\|}$ surface for strong and weak B.
Fig. B.8	The $\kappa_{\perp}$ surface for strong and weak B.

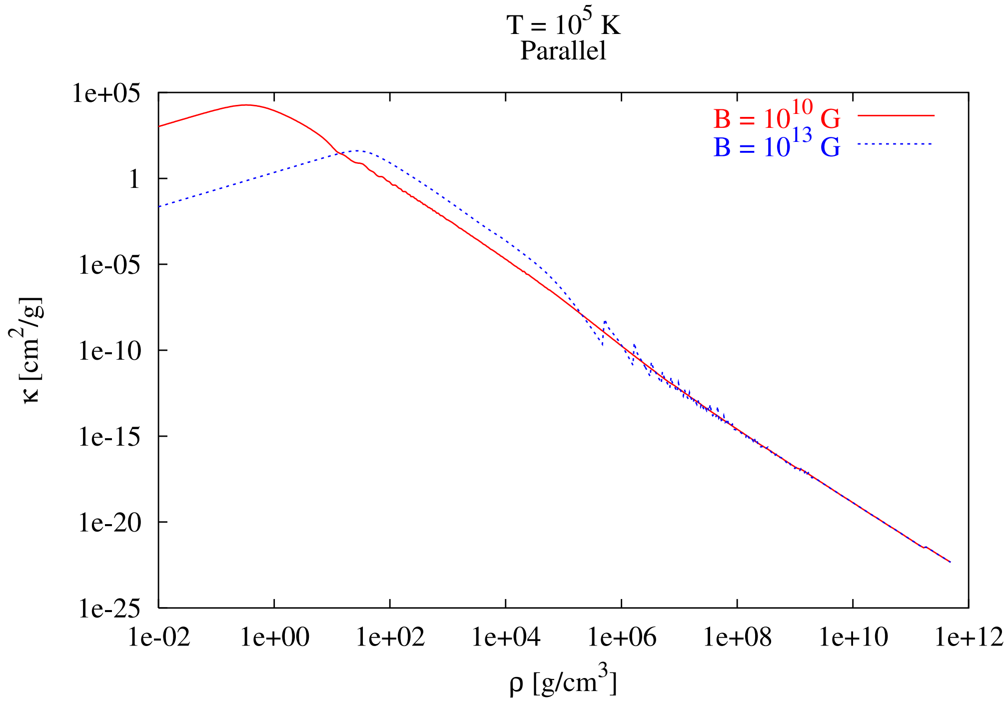

Figure B.1: The total opacity in the parallel case at low ($T = 10^5$ K.) temperature. Shown are the curves for $B = 10^{10}$ and $B = 10^{13}$ G.

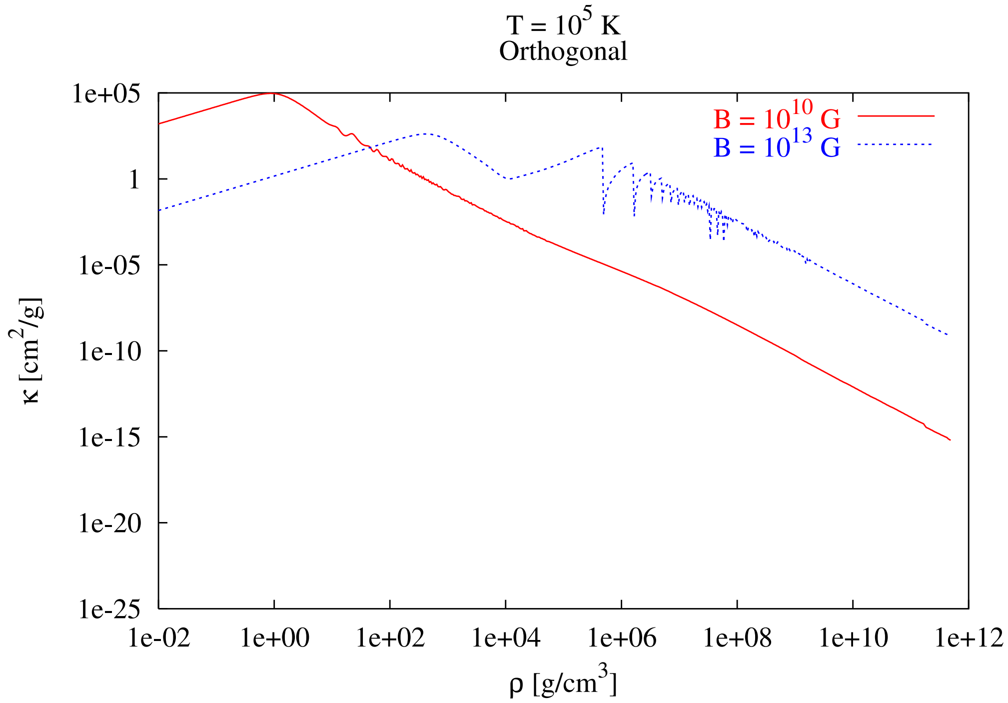

Figure B.2: The total opacity in the orthogonal case at low ($T = 10^5$ K.) temperature. Shown are the curves for $B = 10^{10}$ and $B = 10^{13}$ G.

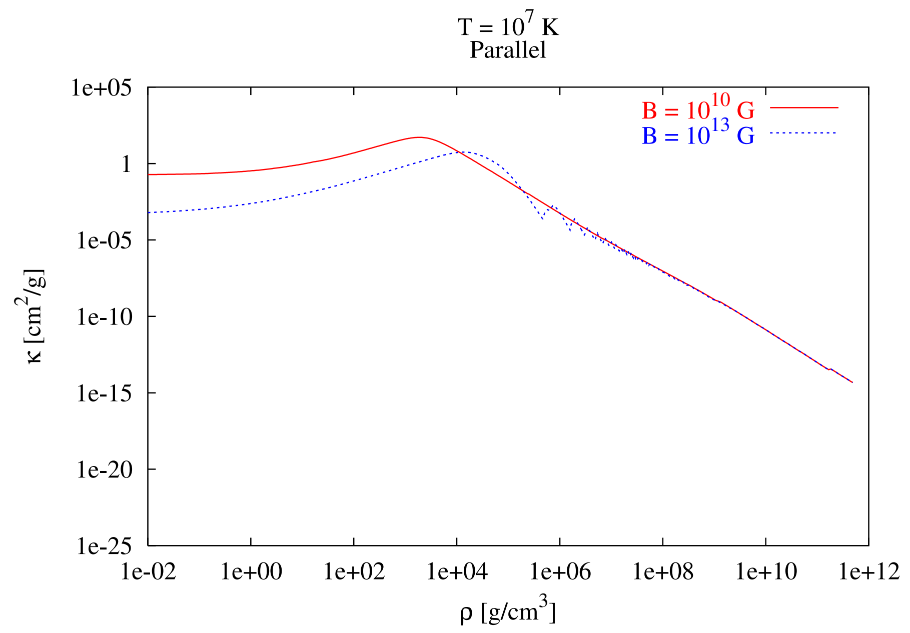

Figure B.3: The total opacity in the parallel case at medium ($T = 10^7$ K.) temperature. Shown are the curves for $B = 10^{10}$ and $B = 10^{13}$ G.

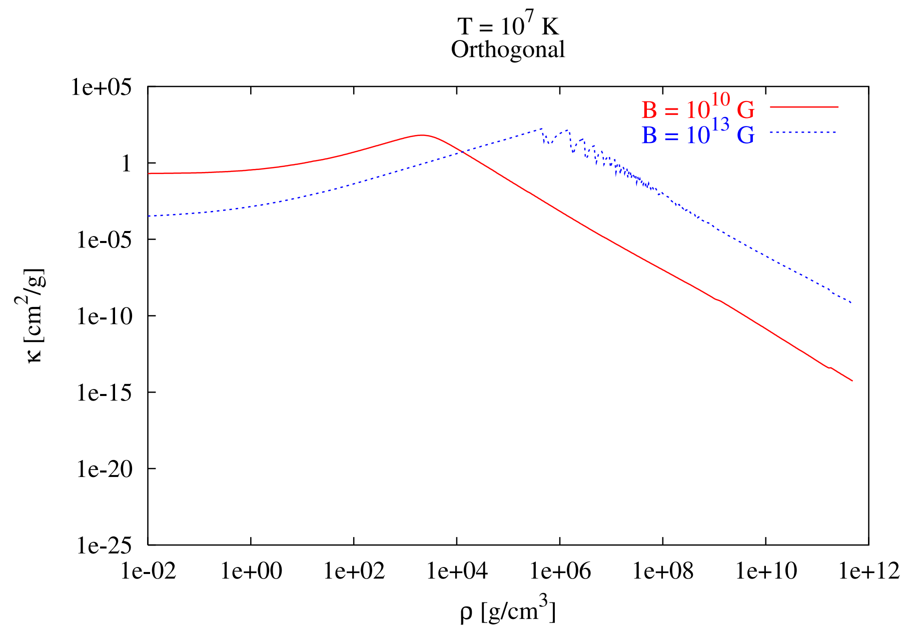

Figure B.4: The total opacity in the orthogonal case at medium ($T = 10^7$ K.) temperature. Shown are the curves for $B = 10^{10}$ and $B = 10^{13}$ G.

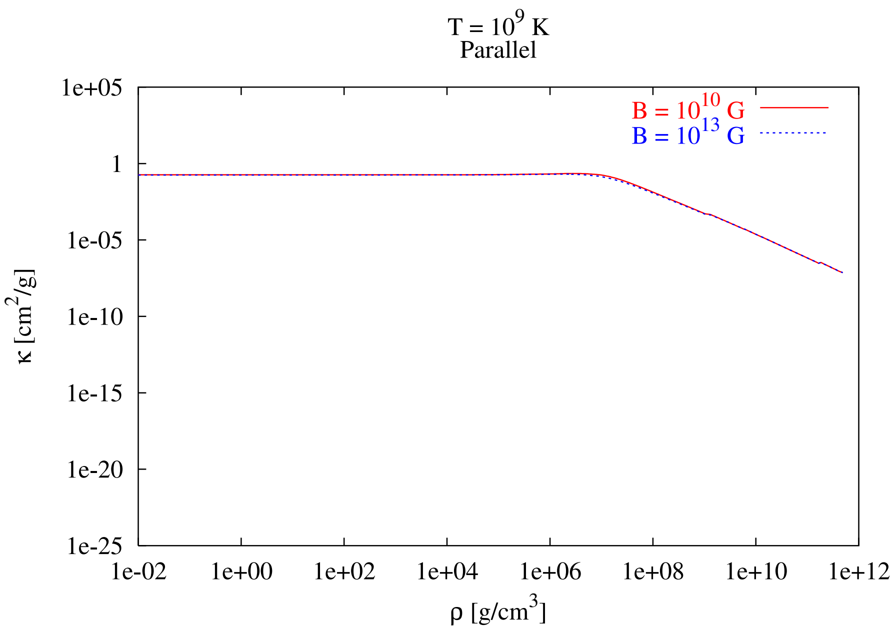

Figure B.5: The total opacity in the parallel case at high ($T = 10^9$ K.) temperature. Shown are the curves for $B = 10^{10}$ and $B = 10^{13}$ G.

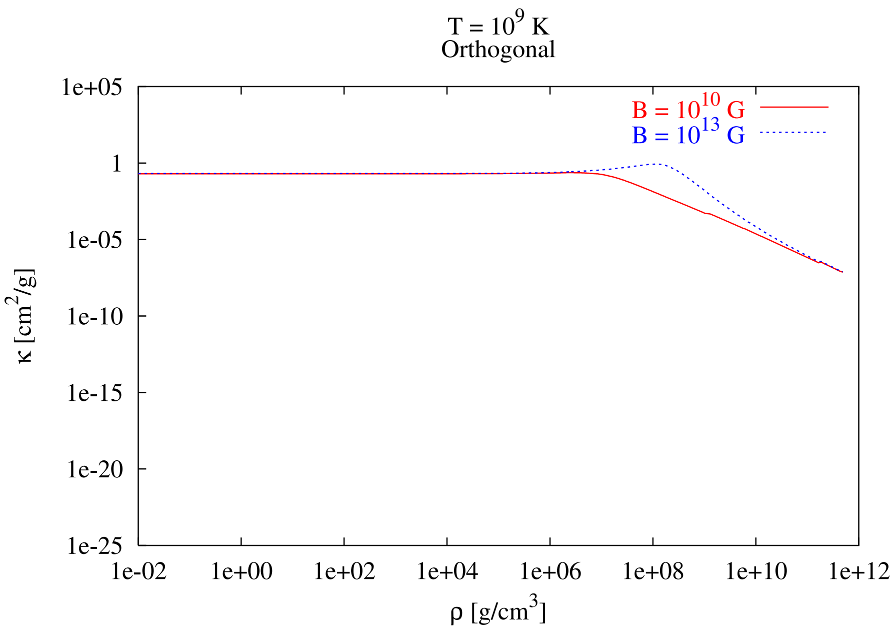

Figure B.6: The total opacity in the orthogonal case at high ($T = 10^9$ K.) temperature. Shown are the curves for $B = 10^{10}$ and $B = 10^{13}$ G.

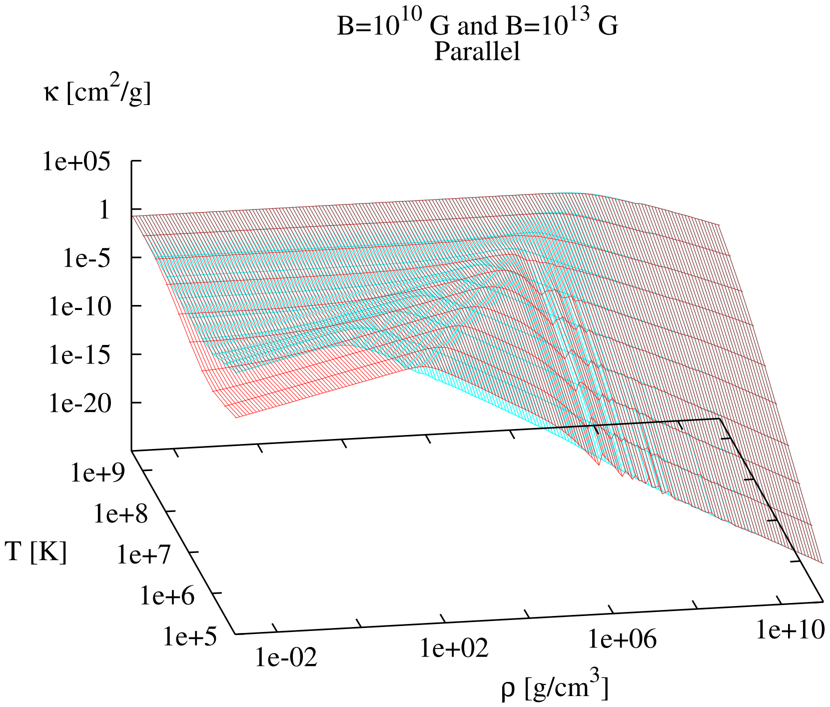

Figure B.7: The total opacity surface in the parallel case. Shown are the surfaces for $B = 10^{10}$ and $B = 10^{13}$ G.

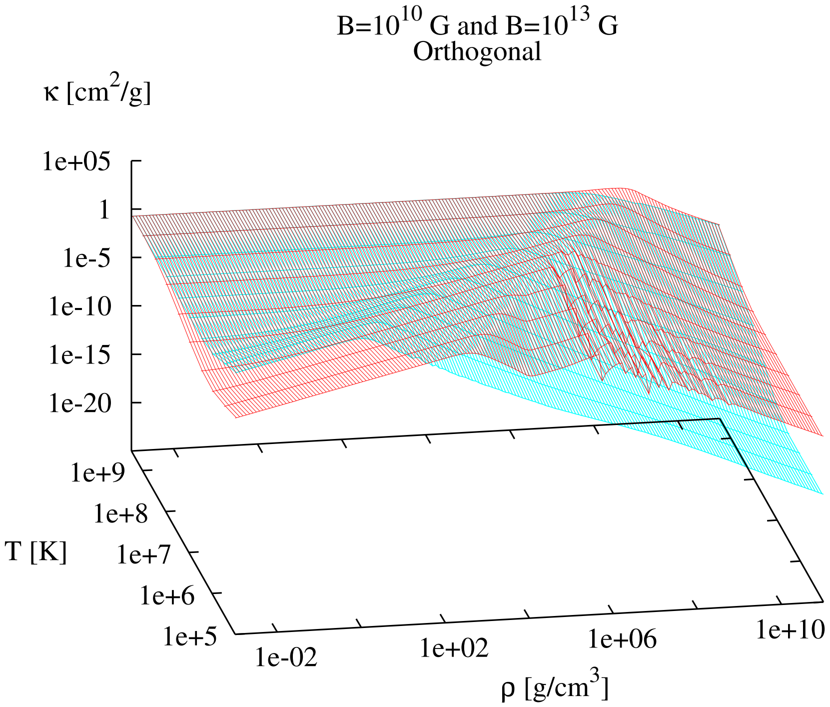

Figure B.8: The total opacity surface in the orthogonal case. Shown are the surfaces for $B = 10^{10}$ and $B = 10^{13}$ G.

Bibliography

[1] G. Baym, C. Pethick, and P. Sutherland. The ground state of matter at high densities: Equation of state and stellar models. *Astrophysical Journal*, 170:299–317, 1971.

[2] P. A. Caraveo. A sociological study of the optically emitting isolated neutron stars. *Preprint*, astro-ph/0001112, 2000.

[3] Patrizia A. Caraveo, Giovanni F. Bignami, and Joachim E. Trümper. Radio-silent isolated neutron stars as a new astronomical reality. *The Astronomy and Astrophysics Review*, 7:209–216, 1996.

[4] Bradley W. Carrol and Dale A. Ostlie. *Modern Astrophysics*. Addison-Wesley Publishing Company Inc, Reading, Massachusetts, 1996.

[5] Gillies Chabrier, Alexander Y. Potekhin, and Dmitry G. Yakovlev. Cooling neutron stars with accreted envelopes. *Astrophysical Journal*, 477:L99–L102, 1997.

[6] P. P. Eggleton, J. Faulkner, and B. Flannery. An approximate equation of state for stellar material. *Astronomy & Astrophysics*, 23:325–330, 1973.

[7] E. H. Gudmundsson, C. J. Pethick, and R. I. Epstein. Neutron star envelopes. *Astrophysical Journal*, 259:L19–L23, 1982.

[8] E. H. Gudmundsson, C. J. Pethick, and R. I. Epstein. Structure of neutron star envelopes. *Astrophysical Journal*, 272:286–300, 1983.

[9] Einar H. Gudmundsson. *Neutron Star Envelopes and the Cooling of Neutron Stars*. PhD thesis, University of Copenhagen, August 1981.

[10] H. Heiselberg and V. Pandharipande. Recent progress in neutron star theory. *Preprint:*, astro-ph/0003276, 2000.

[11] Lars Hernquist. Thermal structure of magnetized neutron-star envelopes. *Monthly Notices of the Royal Astronomical Society*, 213:313–336, 1985.

[12] Jeremy S. Heyl and Lars Hernquist. Almost analytic models of ultramagnetized neutron star envelopes. *Monthly Notices of the Royal Astronomical Society*, 300:599–615, 1998.

[13] F. K. Lamb. Neutron stars and black holes. In D. L. Lambert, editor, *Frontiers of Stellar Evolution*, pages 299–388, Los Angeles, 1991. Astronomical Society of the Pacific.

[14] J. M. Lattimer and M. Prakash. Neutron star structure and the equation of state. *Preprint*, astro-ph/0002232, 2000.

[15] Kenneth Van Riper. Magnetic neutron star atmospheres. *Astrophysical Journal*, 329:339–375, 1988.

[16] Dany Page. Surface temperature of a magnetized neutron star and interpretation of the ROSAT data. I. dipolar fields.

[17] Dany Page. Thermal evolution of isolated neutron stars. In A. Alpar, R. Buccheri, and J. van Paradijs, editors, *The Many Faces of Neutron Stars*, page 539, Boston, 1998. Kluwer Academic Publishers.

[18] A. Y. Potekhin. Electron conduction in magnetized neutron star envelopes. *Astronomy & Astrophysics*, 351:787–797, 1999.

[19] A. Y. Potekhin, G. Chabrier, and D. G. Yakovlev. Internal temperatures and cooling of neutron stars with accreted envelopes. *Astronomy and Astrophysics*, 323:415–422, 1997.

[20] A. Y. Potekhin and D. G. Yakovlev. Thermal structure and cooling of neutron stars with magnetized envelopes. *Preprint (submited to Astronomy & Astrophysics)*, astro-ph/0105261, 2001.

[21] William H. Press, Saul A. Teukolsky, William T. Vetterling, and Brian P. Flannery. *Numerical Recipies in Fortran, Second Edition.* Cambridge University Press, Cambridge, 1986.

[22] Ö. E. Rögnvaldsson, I. Fushiki, E. H. Gudmundsson, C. J. Pethick, and J. Yngvason. Thomas-Fermi calculations of atoms and matter in magnetic neutron stars: Effects of higher Landau bands. *Astrophysical Journal*, 416:276–290, 1993.

[23] Stuart L. Shapiro and Saul A. Teukolsky. *Black Holes, White Dwarfs, and Neutron Stars*. Wiley-Interscience, New York, 1983.

[24] N. A. Shilant'ev and D. G. Yakovlev. Radiative heat transfer in surface layers of neutron stars with a magnetic field. *Astrophysics and Space Science*, 71:45–50, 1980.

[25] Christopher Thompson and Robert C. Duncan. The soft gamma repeaters as very strongly magnetized neutron stars- I. radiative mechanism for outbursts. *Monthly Notices of the Royal Astronomical Society*, 275:255–300, 1995.

[26] A. Thorolfsson, Ö. E. Rögnvaldsson, J. Yngvason, and E. H. Gudmundsson. Thomas-Fermi calculations of atoms and matter in magnetic neutron stars. II. finite temperature effects. *Astrophysical Journal*, 502:847–857, 1998.

[27] J. Ventura and A. Y. Potekhin. Neutron star envelopes and thermal radiation from the magnetic surface. *Preprint*, astro-ph/0104003, 2001.